Nonvesicular trafficking by a ceramide-1-phosphate transfer protein regulates eicosanoids

Supplementary Information

- **Supplementary Results and Discussion**
- **Supplementary Methods**
- **Supplementary References**
- **Supplementary Tables (Table S1-S5)**
- **Supplementary Figures legends**
- **Supplementary Figures (Figure S1- S14)**

SUPPLEMENTARY RESULTS AND DISCUSSION

Sphingosine-in and Sphingosine-out Binding Modes with Different C1P Species

Sphingosine-in binding modes are observed upon severe shortening of the C1P acyl chain (2:0-C1P/CPTP; Fig. 3c,d, Supplementary Fig. S3a, S4e; Table 1) or introduction of *cis* mono-unsaturation (18:1-C1P/CPTP; Fig. 3a,b; Supplementary Fig. S3f; S4d; Table 1). The small acetyl acyl chain in 2:0-C1P (Fig. 3c) enables the sphingosine chain to bend in a serpentine way within the pocket (Fig. 3d; Supplementary Fig. S3a, S4e) so that the C10, C11 and C12 carbons cross over into the same space occupied by the acyl chain in 16:0-C1P/CPTP.

In the 8:0-C1P/CPTP complex, the outwardly projecting sphingosine chain lacks stabilization by partner protein leading to structural flexibility and loss of electron density for the last six carbons of the sphingosine chain (Fig. 3e,f, Supplementary Fig. S3b; S4f; Table S1). The smaller acyl chain of 8:0-C1P necessitates less expansion and volume change to the hydrophobic pocket and residues near the bottom of the pocket undergo less conformational change.

Nonproductive Binding Interaction between CPTP and Phosphatidic Acid (PA), a glycerolipid analog of C1P

Structure determination of di12:0-PA/CPTP complex (Supplementary Fig. S5a-e; Table S1) elucidated the molecular basis of PA non-transfer. PA occupies the same binding site as C1P and is anchored between the phosphate oxygen atoms and K60, R97, R106 and R110 via a hydrogen bond network (Supplementary Fig. S5b-d). Yet, the network is distorted and K60 hydrogen bonding is single rather than bifurcated. The C1-linked chain localizes in the hydrophobic pocket (Supplementary Fig. S5b). The C2-linked chain assumes a sphingosine-out like conformation. The lack of the acyl-amide moiety results in no hydrogen bonding with D56, distorting the positioning of both PA chains. The distortions obstruct K60 interaction with the bonding O1 atom of phosphate, further loosening PA binding. Superpositioning the lipid phosphates in di12:0-PA/CPTP and 12:0-C1P/CPTP illustrates the differences (Supplementary Fig. S5e), which lead to much lower SA volume (110 $Å^3$ vs 261 $Å^3$) for di12:0-PA/CPTP compared to sphingosine-out 12:0-C1P/CPTP. The distorted interaction mitigates PA transfer by CPTP (Supplementary Fig. S5f-h). The lack of an acyl-amide linkage in S1P may also contribute to its non-transfer by CPTP.

CPTP Mechanism of C1P Uptake/Release During Membrane Interaction

Membranes are likely to facilitate the uptake/release of C1P by providing a two-dimensional organizational platform that acts as a reversible and transient docking site for CPTP while also effectively concentrating the C1P lipid ligand. Modeling of CPTP-membrane interactions by the Orientation of Protein in Membrane prediction algorithm[1] indicates that I49 and F52 of the α1-α2 loop region as well as W152, V153 and V60 of the α5-α6 region are likely to act as lipid bilayer insertion points when CPTP partitions to the membrane (Supplementary Fig. S6c,d). The shallow insertion depth and minimal perturbation resulting from membrane translocation reveal CPTP to be a peripheral, amphitropic membrane protein. The six basic surface residues (K55, R62, R66, R97 R155, R156) present near the C1P-binding site are expected to interact with negatively-charged phospholipid headgroup moieties within the membrane surface. The conserved orientation of C1P upon binding to CPTP is not altered by changing the C1P acyl chain length from 2 to 18 carbons and can be traced to the 'pincher-like' clasping by D56 and H150, which hydrogen bond to the respective amide group nitrogen and oxygen atoms in ceramide. This conserved orientation of bound C1P accounts for sphingosine being the chain remaining outside the hydrophobic pocket (Supplementary Fig. S6b). In fact, the 'sphingosine-out' binding mode could represent a 'transition-state intermediate' of the lipid transfer process (Supplementary Fig. S6d), an idea supported by the enhanced mobility of the sphingosine chain and nearby helix-6 (Supplementary Fig. S6a,b). The sphingosine chain would be expected to help tether CPTP to the membrane during C1P loading (or unloading). Upon entry of both chains into the hydrophobic pocket (Supplementary Fig. S6c), release from the membrane is expected to be favorable enabling the lipid carrier function of CPTP to ensue.

Comparison of CPTP with Other Lipid phosphate-binding folds

Compared to other proteins known to bind lipids containing single-phosphate headgroups, the CPTP binding motif is previously unknown. Sphingosine-1-phosphate (S1P) lyase utilizes a 'phosphate cup' containing Tyr, His, and Ser along with one Arg, to accomplish S1P binding and hydrolysis[2]. In contrast, humanized monoclonal antibody Fab fragment achieves S1P binding by using two Ca^{++} ions to bridge between phosphate oxygens and Asp residues while also hydrogen bonding via Glu, Ser, and Gly to the lipid's hydroxyl moieties[3]. Docking models for S1P or its related immunosuppressive analog FTY720 into S1P1 and S1P3 receptors, based on threading

with the crystallographic coordinates of rhodopsin, show binding sites containing only single Arg residues along with Glu and either Leu or Phe[4]. In the case of cPLA$_2$α, C1P activates by binding "head-first" to a β-groove containing three sequential basic residues (Arg57, Lys58 and Arg59), with the exposed ceramide chains acting to tether the phospholipase to the membrane and lowering membrane dissociation, thus enhancing the generation of arachidonic acid for eicosanoid production[5]. A similar linear motif of cationic residues is observed in the mechano-sensitive channel of large conductance MscL, which carries a cluster of three basic amino acids (Arg98, Lys99, and Lys100) on its cytosolic face and interacts with PA[6]. CPTP shares few similarities with the 'venus flytrap' fold that characterizes the phosphate-binding protein superfamily[7], where two globular domains consisting of a central β-sheet core, hinge together to create a phosphate-binding site accessible only by large conformational changes[8].

In both apo- and holo-CPTP, cationic residues of the phosphate headgroup recognition site are relatively fixed and C1P binding triggers minimal conformational change. The stability and high pK values are expected to aid C1P binding across a relatively broad pH range. In contrast, conformational flexibility and pH sensitivity are hallmarks of the ubiquitous Gly-rich loops [GxGxxG] and P-loops [GxxxxGKS/T] that bind phosphate in unrelated NADP/NAD and ATP/GTP binding proteins[9-11]. Thus, all evidence indicates that CPTP conformational architecture represents a new kind of lipid phosphate binding fold.

Structural Comparison of CPTP and CERT

Perhaps the most surprising structural revelation about CPTP is its complete lack of global conformational homology with ceramide transfer protein (CERT), which consists of a N-terminal pleckstrin homology (PH) domain, a middle coiled domain containing a FFAT motif and a C-terminal START domain that binds ceramide (Supplementary Fig. S7a). The CERT START domain has the same overall helix-grip structure as other START domains, consisting of two helices at the N- and C-termini separated by nine β-strands and two shorter helices (Supplementary Fig. S7b)[12-14]. A long cavity, composed of curved β-sheets and covered by three α-helices and two Ω loops, runs through the center of the CERT START domain. This amphiphilic cavity is large (~2016 Å^3), pre-existing, and lined by 26 nonpolar and 10 polar and/or charged residues. Five of the polar/charged residues are buried deep in the cavity where they form hydrogen bonds with the hydroxyl and amide groups of the ceramide headgroup

region, while the hydrocarbon chains point back toward the surface (Supplementary Fig. S7b,c). Thus, the structural basis for specific recognition and binding of ceramide by the START domain of CERT differs dramatically from C1P binding by CPTP. No extra space exists at the bottom of the START cavity to accommodate a polar group bulkier than the C1 hydroxyl headgroup of ceramide, an arrangement strikingly different from CPTP where the positively-charged cavity on the protein surface enables unobstructed access of the bulky, hydrated phosphate headgroup of C1P (Fig. 2a,f,g). Structural studies of CERT complexed with ceramide species having acyl chains with different lengths show both the sphingosine and acyl chains completely buried within the START binding cavity, but with unoccupied cavity space persisting when the acyl chain is short (e.g. 6:0 Cer)[12]. The orientation of ceramide in CERT is reversed compared to C1P in CPTP in that the ceramide headgroup is buried deeper than its hydrocarbon chains inside the START binding cavity (Supplementary Fig. S7b,c) suggesting a fundamentally different mechanism of ceramide uptake and release during membrane interaction compared to CPTP.

Structural Comparison of CPTP and GLTP

Despite having only 17% sequence identity (Supplementary Fig. 1a), CPTP and GLTP share similar two-layer, α-helically dominated, global topologies that feature remarkably different lipid specificities. The most obvious difference is the presence of an additional α-helical segment (αN) at the N-terminus of CPTP (Fig. 1f-h). Also, superpositioning of bound lipid in GLTP and CPTP indicates lateral displacement of the binding pockets relative to each other (Supplementary Fig. S8a,b). In CPTP, the hydrophobic pocket is positioned closer to the interior core of the protein due to differences in helical movements during lipid acquisition. Other important differences are the following: i) All key residues implicated in sugar recognition by GLTP differ from those that recognize phosphate in CPTP (Supplementary Fig. S8c). The only shared residues specifically involved in lipid recognition are the Asp and His residues that hydrogen bond with the amide nitrogen and oxygen atoms of the ceramide moiety consistent with the preference of both proteins for ceramide-based lipids; ii) Structural superposition of GLTP bound to LacCer[15] and CPTP bound to 16:0-C1P shows that the surface cavity for lipid headgroup binding is much smaller, more pit-like, and very basic (cationic) in CPTP (Supplementary Fig. S8d) compared to GLTP (Supplementary Fig. S8e). These structural differences explain the highly selective binding of C1P by CPTP compared to the broader selectivity of GLTP for glycosphingolipids

having headgroups with various sugar combinations[16,17]; iii) The presence of the novel αN-helix, positioned across the bottom of the hydrophobic tunnel, seals it and imparts more absolute pocket-like character to CPTP compared to the tunnel-like quality of the GLTP cavity[18,19]. The net effect of the αN-helix location and the translational displacement of the CPTP hydrophobic pocket seem to be functional selectivity of CPTP for C1P species with acyl chains of 16 to 18 carbons. The terminal methyl groups of the 18:1 and 16:0 acyl chains localize at similar depths near the bottom of the hydrophobic pocket in close proximity to Leu10 of the αN-helix (Fig. 3b). These features distinguish the CPTP hydrophobic pocket from that of GLTP, which has a narrow extended bottom region that enables accommodation of long acyl chains (e.g. 24:1), and occupation by extraneous hydrocarbons when the acyl chain is short[17,18].

Biological Significance of CPTP in Sphingolipid Metabolism

Currently, little is known about the catabolism of C1P in mammals[20,21] . Two scenarios appear plausible: dephosphorylation of C1P by a lipid phosphate phosphatase leading to the production of ceramide; or deacylation to sphingosine-1-phosphate. Our data demonstrating that siRNA mediated down-regulation of CPTP significantly affects the intracellular levels of sphingosine-1-phosphate (Supplementary Fig.S10b) and sphingosine (Supplementary Fig. S10c), but with little effect on ceramides (Supplementary Fig. S10d), points to deacylation rather than dephosphorylation, as a likely catabolic pathway for C1P. Nonetheless, C1P catabolism via dephosphorylation cannot be excluded based solely by the lack of dramatic change in ceramide upon mitigation of CPTP-mediated C1P transfer. Changes to ceramide originating from the C1P pool could simply be too minuscule to appreciably impact the total cellular ceramide pool. Ceramide also can be rapidly converted to more complex sphingolipids such as SM and hexosylceramides[20]. In fact, minor but significant effects on these sphingolipids are observed upon modulation of CPTP and CERK expression. Together, our data suggest that CPTP expression profoundly affects C1P synthesis, which in turn plays a complex and enigmatic role in regulating sphingolipid synthesis.

The complex and mysterious metabolic role of C1P is illustrated by siRNA-mediated down-regulation of CPTP, which results in modest but measurable reduction in various species of the large cellular sphingomyelin (SM) pool (Supplementary Fig. S10e), suggesting one of two possibilities. CPTP could transfer C1P to a site where it exerts an inhibitory effect on SM degradation, a scenario in agreement with the findings of Gómez-Muňoz *et al*[22] showing

inhibition of aSMase activity by C1P. It appears that diminished trafficking of C1P via down-regulation of CPTP prevents C1P-mediated inhibition of aSMase or another SMase isoform, leading to increased SM catabolism. The recent finding of ADAM17 activity regulation by C1P downstream of aSMase[23] also supports this scenario. Another possibility could be CPTP transport of C1P to a site where it is metabolized into SM. But this seems unlikely because the SM acyl chain lengths affected by CPTP down-regulation differ from those of the C1P subspecies affected in the same experiments. In any case, the concomitant decreases in sphingosine and sphingomyelin induced by CPTP knockdown are consistent with the reported inhibition of ER-located serine palmitoyltransferase[24] and lysosomal acid SMase[22] by C1P. Additional studies will be needed to assess the involvement of CPTP at these subcellular sites as well as the functional aspects of CPTP-controlled C1P levels at the nucleus.

A role for C1P in regulating the metabolism of hexosylceramides is suggested by the increase in monohexosyl ceramides observed upon down-regulation of CERK expression (Supplementary Fig. S10f). We originally surmised this to be the inhibitory action of C1P on acid SMase leading to an increase in ceramide, which presumably is "shunted" into the monohexosyl ceramide "pool" as a defense mechanism against apoptosis. However, the opposite effect is not observed upon increasing intracellular C1P by inhibiting CPTP-mediated transfer suggesting a more complex effect of C1P on monohexosyl ceramide production than expected. The inhibitory mechanism appears to depend upon a minimum threshold level of C1P since elevation of C1P by blocking its trafficking does not result in decreases in the 16:0- and 24:0-monohexosyl ceramides. Thus, it is possible that a decrease of C1P at its site of synthesis caused by altered trafficking could explain the elevations in monohexosyl ceramides with the same chain lengths.

As reported in the main text, CPTP depletion shows dramatic alterations in Golgi cisternal stack morphology via fragmentation by 24 h but no apparent effect on other subcellular structures/organelles (Supplementary Fig. S11). The fragmentation is observed with anti-GM130 (*cis*-Golgi marker) and TGN-46 (*trans*-Golgi marker; integrally associated), but presents as more diffuse staining by p230/GCC185 (*trans*-Golgi marker; peripherally associated) consistent with fragmentation-related release from TGN membranes. The findings suggest CPTP expression is essential for maintaining proper Golgi organization by safeguarding localized C1P levels. Despite the fragmentation of Golgi cisternal stacks, the intracellular sites containing

altered C1P levels following CPTP RNAi-knockdown and obtained by subcellular fractionation are expected to be cogent because the approach relies on differences in membrane vesicle density and fractionation by centrifugation, an approach previously used to identify intracellular membranes enriched in CERK[25]. Heavy membranes (HM) are enriched in mitochondria, *trans*-Golgi, and endosomal membranes. Light membranes (LM) are enriched in *cis*-Golgi and ER membranes. The enrichments were confirmed by SDS-PAGE/Western blotting (Supplementary Fig. S13b) using organelle markers for: nuclei (anti-lamin AC), *trans*-Golgi (anti-TGN46), ER (anti-protein disulfide isomerase, PDI), and plasma membrane (anti-caveolin-1). CPTP is detected in the heavy membrane fraction which is enriched in *trans*-Golgi/TGN, a localization site where CERK produces C1P and for cycloxygenases (COX-1/COX-2) during eicosanoid production[26,27]. Nonetheless, the presence of *cis*-Golgi membranes in our heavy membrane fraction remains a possibility. Because our microscopy data show no co-localization of CPTP to mitochondria (which also is enriched in the heavy membrane fraction), we conclude that CPTP-knockdown-induced increase of C1P in the heavy membrane fraction reflects CPTP depletion at the Golgi complex, a localization site supported by microscopy (Fig. 4g). Taken together, the data suggest that when CPTP is depleted and inadequately localized to the *trans*-Golgi/TGN: i) C1P accumulates in the Golgi complex and decreases at the plasma membrane; and ii) pro-inflammatory eicosanoid production is initiated by cPLA$_2\alpha$ at the Golgi. CPTP depletion also profoundly alters Golgi morphology and possibly its function. It is noteworthy, however, that other lipids destined for the plasma membrane, i.e. SM, by vesicular transport after production in the Golgi are unaffected by CPTP depletion (Supplementary Fig S13 figure legend). We thus conclude that C1P elevation in the Golgi induced by CPTP depletion is specific and consistent with CPTP involvement in C1P transfer from the Golgi complex to the plasma membrane.

SUPPLEMENTARY METHODS

CPTP (GLTPD1) Cloning and Transcript Analysis in Tissues

Human brain cDNA library (Clontech) was amplified using Herculase II fusion DNA polymerase and 5'-ATGGATGACTCGGAGACAGGTTTCA-3'/5'-CTAGGGCAGGTCCAG-CAGGGAG-3' was used for *CPTP* ORF amplification (98°C, 20 s; 63°C, 20 s; 72°C 45 s; 38 cycles). PCR products were separated on a 1.2% agarose gel, purified, cloned into T-vector (Promega) and sequenced. Point mutations were generated by QuikChange® site-directed

mutagenesis (Stratagene). All mutant plasmid constructs were verified by DNA-sequencing. To assess mRNA expression, two human multiple tissue cDNA (MTC) panels were used as PCR templates according to the manufacturer's instructions (Clontech). Linear amplification was performed. The sense and antisense primers for *CPTP* and PCR temperature cycle settings were the same as for *CPTP* ORF cloning. Amplification of *G3PDH* housekeeping transcript involved 24 cycles using specific primers 5'-TGAAGGTCGGAGTCAACGGATTT-GGT-3' and 5'CATGTGGG-CCATGAGGTCCACCAC-3'. PCR products (*CPTP* and *G3PDH)* were electrophoresed on 1.2% agarose gels.

Heterologous Protein Expression and Purification

GLTPD1 ORFs encoding human and mouse (GenBank JN542538; NP_077792.2) CPTP were cloned in pET-Sumo vector (Invitrogen), overexpressed, and affinity purified as described in the on-line Methods.

CPTP Lipid Transfer Activity Involving Membrane Vesicles

Intermembrane lipid transfer by CPTP was measured in real time by Förster resonance energy transfer (FRET). Donor POPC vesicles, containing 1 mole% AV-lipid (acyl chain omega-labeled with anthrylvinyl fluorophore, [(11*E*)-12-(9-anthryl)-11-dodecenoyl]) and 1.5 mole% 1-acyl-2-[9-(3-perylenoyl)-nonanoyl]-3-*sn*-glycero-3-phosphocholine [Per-PC] were prepared by rapid ethanol injection[28]. In competition assays[17], donor vesicles also contained competitor lipids at 0.5, 1.0 and 2.0 mole%. Acceptor POPC vesicles were prepared by sonication as described previously[29]. Because both fluorophore lipids are initially present only in the donor vesicles, excitation of the anthrylvinyl (AV) group (370 nm) results in minimal emission because of energy transfer to Per-PC. CPTP addition results in an exponential increase in AV emission intensity (425 nm) as the protein transports AV-C1P away from the donor vesicles (creating separation from the 'nontransferable' Per-PC) and delivers to the pure POPC acceptor vesicles present in 10-fold excess. Lipid transfer kinetics are indicated by the time-dependent increase in emission at 425 nm relative to the baseline fluorescence in the absence of CPTP. Addition of Tween 20 detergent late in the kinetic time course provides the maximum AV intensity achievable upon 'infinite' separation from 3-perylenoyl fluorophore (Supplementary Fig. S1b). Maximum transfer, ΔF, represents the difference in emission intensity in the absence and presence of C1P. The initial lipid transfer rate, $v_{o,}$ is obtained by nonlinear regression analyses

(ORIGIN 7.0 software, Northhampton, MA). The standard deviations are calculated at 95% confidence intervals. *R*2 values for all estimates are >0.96.

Crystallization and Structure Determination

We co-crystallized human CPTP (15 mg/ml) with C1P (2 mM in 50% ethanol stock) using C1P species with various acyl chains (2:0, 8:0, 12:0, 16:0, 18:1). Mouse apo-CPTP (79% aa. sequence identity with human CPTP) was crystallized and structurally resolved (2.55 Å, Table S2; Supplementary Fig. S2d) when extensive crystallization trials with human apo-CPTP were unfruitful. Superposition of the apo- and 16:0-C1P bound CPTP structures shows a rmsd of 1.4 Å (Supplementary Fig. S2e). Co-crystallization of human CPTP with di8:0, di12:0, di16:0 and di18:0 phosphatidic acid (PA) was attempted but well-diffracting crystals were obtained only for CPTP complexed with di12:0-PA. All lipids for co-crystallization were purchased from Avanti Polar Lipids. Crystallization hits from initial screens were optimized by the hanging drop vapor diffusion method by systematically varying the pH and individual component concentrations. Conditions that yielded crystals are summarized in Table S3. For data collection, crystals were flash frozen (100 K) in reservoir solutions supplemented with 20% (v/v) ethylene glycol. Diffraction data sets were collected on 24-ID-C and 24-ID-E beamlines at the Advanced Photon Source (APS) and X29A beamline at Brookhaven National Laboratory. Data sets were integrated and scaled using the HKL2000 suite[30]. Interestingly, all crystals belonged to different crystal forms. For phasing, SAD (*S*ingle-wavelength Anomalous Dispersion) data were collected for the Se-Met labeled crystal of human CPTP in complex with 8:0-C1P at Se peak wavelength (statistics in Table S2)[31]. The statistics for data collection, refinement and SAD phasing are provided in Tables S1 and S2.

Structure Determination

The crystal structure of SeMet-labeled human CPTP in complex with 8:0-C1P was solved by single-wavelength anomalous dispersion (SAD) implemented in the Phenix program suite. The 24 selenium sites (6 Se per molecule and 30 total Se in the asymmetric unit) and the non-crystallographic symmetry operations were identified and the phases were calculated using Phenix.autosol[32]. Density modification and automatic model building were carried out using the Phenix.autobuild[33] which was able to build >60% of the polypeptide chain for the 6 molecules in the asymmetric unit. The model was further improved using iterative cycles of manual model

building in Coot[34] and refinement using Phenix.refine[35] (statistics for data collection and SAD phasing in Table S2). The structures of all complexes of human CPTP as well as mouse apo-CPTP were solved by molecular replacement using MOLREP[31] in the CCP4 suite and using Se-CPTP structure as a search model.

Model Building and Refinement

Model building and refinement for all structures were performed using Coot and Phenix.refine, respectively[34,35]. Refinement was monitored with the R_{free} value calculated for a randomly selected 5-10% of reflections in the data set. After initial round of refinement, difference Fourier maps showed distinct electron density for the lipid molecules. Lipid molecules were docked into the electron density and the complex was further refined. Omit maps were used to confirm the placement and conformation of the ligand in the complex structures (Supplementary Fig. S3 a-g). Geometric coordinates and stereochemical libraries for 2:0-, 8:0-, 12:0-, 16:0-, and 18:1-C1P and di12:0-PA were prepared using PRODRG[36] and Phenix.elbow[37]. Water molecules and alternative conformations of amino acids were added using Coot. The final structure was analyzed by PROCHECK [37] and details of the data collection and refinement statistics are shown in Table S1.

Structure Analysis

Secondary structural elements were assigned using DSSP (http://swift.cmbi.ru.nl/gv/dssp/). Electrostatic surface potentials were calculated with GRASP[38]. Amino acid residues interacting with the lipid molecule are according to LIGPLOT analysis[39]. The estimated solvent-accessible volumes of cavities C1P/PA bound human CPTP were calculated by CASTp program[40]. The interaction of CPTP with the membrane was analyzed using the orientation of proteins in membranes (OPM) computational approach[1]. The secondary structure matching (SSM) algorithm implemented within Coot was used for superpositioning different structures and for rmsd calculations[41]. Figures were generated with PyMOL[42]. Superposition of structures for CPTP obtained with C1P containing different lengths of acyl chains showed similar overall conformation with rmsd values ranging from 0.8-1.0 Å.

RNAi Duplexes used for CPTP depletion

GLTPD1 OnTargetPlus siRNA (Dharmacon; cat# L-032710-02-0005) consisting of the following sense sequences (UGACAGAGAAGGUGGCGAC, GAGACAGGUUUCAAUCUGA,

CCCAGAAGCUCUACGCCGA, CCAGCAGACAUGCGAGCUU) was used to target the *GLTPD1* ORF and a cocktail of custom sense sequences (AAAAUGAGCCACAGAGCAAUU, CCAGAAAAUGAGCCACAGAUU, GAAAAUGAGCCACAGAGCAUU, GAGCCACAGAGCAAGCUGAUU, was used to target the *GLTPD1*-3'UTR.

Cellular Lipid Extraction

Cell lipids were harvested using a modified Bligh-Dyer protocol[43]. Briefly, the plates were placed on ice, and the media was transferred to another tube and used in the quantitative and qualitative analysis of eicosanoids as detailed below. The cells were washed twice with ice-cold PBS and harvested by scraping in 200 µl of PBS followed by sonication to obtain a homogenous mixture. Lipids were extracted from the remaining cells using a modified Bligh and Dyer method and analyzed as described by Wijesinghe *et al*[43]. Briefly, methanol:chloroform (2:1; 1.5 ml) was added to the cell suspension (PBS; 200 µl). The samples were spiked with 500 pmol of C1P, sphingomyelin, ceramide, and monohexosyl ceramide ($d_{18:1/12:0}$ species) as internal standard (Avanti Polar Lipids). The mixture was sonicated to disperse the cell clumps and incubated for 6h at 48°C. Extracts were then transferred to a new glass tube, dried down and reconstituted in methanol (600 µl) by sonicating and incubating at 48°C for 15 min. The latter step is a new addition to our previously published method[42] and was incorporated to ensure proper solubilization of the long chain sphingolipids. It should be noted that the resulting analyses for ceramide and monohexosyl ceramide species showed increased prominence of the long chain sphingolipids compared to our earlier sphingolipid patterns for A549 cells[43] because of the improvements in the lipid extraction procedure. Because sphingolipid species containing the sphinganine (18:0) base were extremely low, only the data for sphingolipid species containing the sphingosine (18:1) base are shown in Figure 4 and Supplementary Figure S10.

Analysis of Eicosanoids by HPLC ESI-MS/MS

Eicosanoids were analyzed by HPLC ESI-MS/MS in the following way[25]. A 30 min. reversed-phase LC method utilizing a Kinetex C18 column (100 x 2.1mm, 2.6µ) was used to separate the eicosanoids at a 200 µl/min flow rate at 50°C. The column was equilibrated with 100% Solvent A [acetonitrile:water:formic acid (40:60:0.02, v/v/v)] for 5 min and then 10 µl of sample was injected. 100% Solvent A was used for the first minute of elution. Solvent B [acetonitrile:-isopropanol (50:50, v/v)] was increased in a linear gradient to 25% Solvent B to 3 min., to 45%

until 11 min., to 60% until 13 min., to 75% until 18 min., and to 100% until 20 min. 100% Solvent B was held until 25 min., then was decreased to 0% in a linear gradient until 26 min., and then held until 30 min. Eicosanoids were then analyzed using a tandem quadrupole mass spectrometer (ABI 4000 Q-Trap®, Applied Biosystems) via multiple-reaction monitoring in negative-ion mode. Eicosanoids were monitored using precursor → product MRM pairs, which can be found in Supplementary Table S5. The mass spectrometer parameters used were: Curtain Gas: 30; CAD: High; Ion Spray Voltage: -3500V; Temperature: 500°C; Gas 1: 40; Gas 2: 60; Declustering Potential, Collision Energy, and Cell Exit Potential vary per transition.

Confocal and Epifluorescence Microscopy Analyses

BSC-1 cells (African Green Monkey kidney cells; ATCC, Manassas, VA) were cultured in DMEM containing 10% FBS (GIBCO, Grand Island, NY) and 1 mg/ml pen-strep (Sigma-Aldrich, St. Louis, MO) in 10% CO_2. The cells were transfected with EGFP-CPTP (Clontech, Mountain View, CA) using Fugene 6 (Roche Applied Science, Indianapolis, IN), and selected with G418 (2 mg/ml).

Cells on coverslips were fixed in –20 °C methanol and labeled with anti-γ-tubulin (1:1000, rabbit polyclonal, Sigma), followed by secondary antibodies (species appropriate) coupled to Alexa-488, Alexa-594, or Alex-660 at 1:1000 dilution (Invitrogen, Carlsbad, CA). Cells were counter stained with DAPI (Sigma) and mounted in 10% PBS, 90% glycerol. Fixed cells were imaged with a 63 x 1.4 NA apochromatic CS oil immersion objective on a Leica DM RXA2 microscope using a Hamamatsu ORCA-ER CCD camera. Z-stacks (0.2 μm) were compiled as maximum projections. Images were acquired using Simple-PCI software (Compix, Cranberry Township, PA).

Time-lapse images of living cells were captured using a Leica DM RXA2 microscope stand enclosed in a custom-made Plexiglas box maintained at 37°C. Live-cell fluorescence images were captured using a Yokagawa CSU-10 spinning disk confocal head, as modified by McBain Industries (San Diego, CA). Illumination of the fluorescent images was done with a Coherent 488 nm 200mW ‘‘Sapphire’’ continuous wave optically pumped solid-state laser (CW-OPSL) connected by fiber optic cable into the excitation port of the spinning disk confocal head and shuttered through a Ludl MAC5000 shutter controller. Confocal fluorescent images were

acquired through a Leica Plan Apo 63_/1.3 NA glycerol immersion objective and a Hamamatsu 9100 back-thinned ORCA-AG Digital CCD camera, as described by Hornick *et al*[44].

CPTP-siRNAs used to induce Golgi cisternal stack fragmentation (Supplementary Fig. S11) were produced using pSuper.retro.puro vector (gift of Drs. Albert Bendelac & Yuval Sagiv, Univ. Chicago), which we modified further by inserting the enhanced green fluorescent protein (EGFP) ORF at the C-terminus of the puromycin N-acetyl transferase coding sequence (pSuper.puro-egfp). The presence of EGFP coding sequence enabled positive verification of cells transfected with pSuper.retro.puro vector carrying shRNA. Short hairpin RNAs (shRNA) against human CPTP were designed using an on-line siRNA design program (Oligoengine) and subcloned into the BglII/XhoI sites of pSuper.puro-egfp. [CPTPi-3'UTR-fwd, 5'-gatccccGCT-TCCAGAGTGCAATCTAttcaagagaTAGATTGCACTCTGGAAGCtttttc-3'; CPTP-3'UTR-rev, 5'-tcgagaaaaaGCTTCCAGAGTGCAATCTAtctcttgaaTAGATTGCACTCTGGAAGCggg-3'; ScrambledCPTP-3'UTR-fwd, 5'-gatccccGCTTGAACCGAATCTACGTttcaagagaACGTAGAT-TCGGTTCAAGC-tttttc-3'; Scrambled-CPTP-3'UTR-rev, 5'-tcgagaaaaaGCTTGAACCGAATC-TACGTtctcttgaaACGTAGATTCGGTTCAAGCggg-3'] qPCR analyses of siRNA constructs showed ~90% silencing efficiency of the CPTP-RNAi compared to scrambled control.

Subcellular Fractionation

Subcellular fractionation was performed by stepwise centrifugation as described and characterized previously[25] with minor modifications. Treated A549 cells (~3 $\times 10^6$) were disrupted by passage (12x) through a 26 gauge needle. The homogenate was centrifuged (500g, 10 min) to remove unbroken cells followed by 1000g for 10 min to enrich the nuclear membrane-enriched fraction. The post-nuclear supernatant was centrifuged (2,000g, 10 min) to remove residual nuclei and then at 5000g for 10 min to isolate heavy membranes (endosome-/ *trans*-Golgi/mitochondria-enriched). After centrifugation (7000g, 10 min) to remove residual heavy membranes, further centrifugation at 17,000 g for 20 min yielded an ER-/*cis*-Golgi-enriched membrane fraction. The supernatant then was centrifuged at 100,000 g for 1 h to obtain a light membrane fraction enriched in plasma membrane. Fraction enrichment was validated by SDS-PAGE/Western blotting (10 μg/lane) (Supplementary Fig. S13b) using organelle markers for: nuclei (anti-lamin AC; Santa Cruz 1:1000), trans-Golgi (anti-TGN46; AbCam 1:1000), ER (anti-protein disulfide isomerase (PDI); AbCam 1:1000), and plasma membrane (anti-caveolin-1; Santa Cruz 1:1000).

A similar procedure was followed for isolating the internal membrane fractions versus the plasma membrane fractions. After centrifugation at 500 g for 10 min to remove unbroken cells, the resultant supernatant was centrifuged at 17,000 g for 20 min to obtain the total internal membrane fraction. The remaining supernatant was centrifuged at 100,000 g to obtain the plasma membrane-enriched fraction.

SUPPLEMENTARY REFERENCES

1 Lomize, A. L., Pogozheva, I. D., Lomize, M. A. & Mosberg, H. I. Positioning of proteins in membranes: A computational approach. *Protein Sci* **15**, 1318-1333 (2006).

2 Bourquin, F., Riezman, H., Capitani, G. & Grutter, M. G. Structure and function of sphingosine-1-phosphate lyase, a key enzyme of sphingolipid metabolism. *Structure* **18**, 1054-1065 (2010).

3 Wojciak, J. M. *et al.* The crystal structure of sphingosine-1-phosphate in complex with a Fab fragment reveals metal bridging of an antibody and its antigen. *Proc Natl Acad Sci U S A* **106**, 17717-17722 (2009).

4 Rosen, H., Gonzalez-Cabrera, P. J., Sanna, M. G. & Brown, S. Sphingosine 1-phosphate receptor signaling. *Annu Rev Biochem* **78**, 743-768 (2009).

5 Stahelin, R. V., Subramanian, P., Vora, M., Cho, W. & Chalfant, C. E. Ceramide-1-phosphate binds group IVA cytosolic phospholipase a2 via a novel site in the C2 domain. *J Biol Chem* **282**, 20467-20474 (2007).

6 Powl, A. M., East, J. M. & Lee, A. G. Heterogeneity in the binding of lipid molecules to the surface of a membrane protein: hot spots for anionic lipids on the mechanosensitive channel of large conductance MscL and effects on conformation. *Biochemistry* **44**, 5873-5883 (2005).

7 Berna, A., Bernier, F., Chabriere, E., Perera, T. & Scott, K. DING proteins; novel members of a prokaryotic phosphate-binding protein superfamily which extends into the eukaryotic kingdom. *The international journal of biochemistry & cell biology* **40**, 170-175 (2008).

8 Luecke, H. & Quiocho, F. A. High specificity of a phosphate transport protein determined by hydrogen bonds. *Nature* **347**, 402-406 (1990).

9 Hirsch, A. K., Fischer, F. R. & Diederich, F. Phosphate recognition in structural biology. *Angewandte Chemie* **46**, 338-352 (2007).

10 Rossmann, M. G., Moras, D. & Olsen, K. W. Chemical and biological evolution of nucleotide-binding protein. *Nature* **250**, 194-199 (1974).

11 Walker, J. E., Saraste, M., Runswick, M. J. & Gay, N. J. Distantly related sequences in the alpha- and beta-subunits of ATP synthase, myosin, kinases and other ATP-requiring enzymes and a common nucleotide binding fold. *The EMBO journal* **1**, 945-951 (1982).

12 Kudo, N. *et al.* Structural basis for specific lipid recognition by CERT responsible for nonvesicular trafficking of ceramide. *Proc Natl Acad Sci U S A* **105**, 488-493 (2008).

13 Tsujishita, Y. & Hurley, J. H. Structure and lipid transport mechanism of a StAR-related domain. *Nat Struct Biol* **7**, 408-414 (2000).

14 Lavigne, P., Najmanivich, R. & Lehoux, J. G. Mammalian StAR-related lipid transfer (START) domains with specificity for cholesterol: structural conservation and mechanism of reversible binding. *Subcell Biochem* **51**, 425-437 (2010).

15 Malinina, L., Malakhova, M. L., Teplov, A., Brown, R. E. & Patel, D. J. Structural basis for glycosphingolipid transfer specificity. *Nature* **430**, 1048-1053 (2004).

16 Brown, R. E. & Mattjus, P. Glycolipid transfer proteins. *Biochim Biophys Acta* **1771**, 746-760 (2007).

17 Samygina, V. R. *et al.* Enhanced selectivity for sulfatide by engineered human glycolipid transfer protein. *Structure* **19**, 1644-1654 (2011).

18 Malinina, L. *et al.* The liganding of glycolipid transfer protein is controlled by glycolipid acyl structure. *Plos Biol* **4**, 1996-2011 (2006).

19 Airenne, T. T. *et al.* Structural evidence for adaptive ligand binding of glycolipid transfer protein. *J Mol Biol* **355**, 224-236 (2006).

20 Futerman, A. H. Intracellular trafficking of sphingolipids: relationship to biosynthesis. *Biochim Biophys Acta* **1758**, 1885-1892 (2006).

21 Arana, L., Gangoiti, P., Ouro, A., Trueba, M. & Gomez-Munoz, A. Ceramide and ceramide 1-phosphate in health and disease. *Lipids in health and disease* **9**, 15 (2010).

22 Gomez-Munoz, A., Kong, J. Y., Salh, B. & Steinbrecher, U. P. Ceramide-1-phosphate blocks apoptosis through inhibition of acid sphingomyelinase in macrophages. *Journal of lipid research* **45**, 99-105 (2004).

23 Lamour, N. F. *et al.* Ceramide kinase regulates the production of tumor necrosis factor alpha (TNFalpha) via inhibition of TNFalpha-converting enzyme. *J Biol Chem* **286**, 42808-42817 (2011).

24 Granado, M. H., Gangoiti, P., Ouro, A., Arana, L. & Gomez-Munoz, A. Ceramide 1-phosphate inhibits serine palmitoyltransferase and blocks apoptosis in alveolar macrophages. *Biochimica et biophysica acta* **1791**, 263-272 (2009).

25 Lamour, N. F. *et al.* Ceramide kinase uses ceramide provided by ceramide transport protein: localization to organelles of eicosanoid synthesis. *J Lipid Res* **48**, 1293-1304 (2007).

26 Grewal, S., Ponnambalam, S. & Walker, J. H. Association of cPLA2-alpha and COX-1 with the Golgi apparatus of A549 human lung epithelial cells. *J Cell Sci* **116**, 2303-2310 (2003).

27 Leclerc, P., Biarc, J., St-Onge, M., Gilbert, C., Dussault, A-A., Laflamme, C., & Pouliot, M. Nucleobindin co-localizes and associates with cyclooxygenase (COX)-2 in human neutrophils. *PLoS ONE* 3, e2229

28 Mattjus, P., Molotkovsky, J. G., Smaby, J. M. & Brown, R. E. A fluorescence resonance energy transfer approach for monitoring protein-mediated glycolipid transfer between vesicle membranes. *Anal Biochem* **268**, 297-304 (1999).

29 Malakhova, M. L. *et al.* Point mutational analysis of the liganding site in human glycolipid transfer protein. Functionality of the complex. *J Biol Chem* **280**, 26312-26320 (2005).

30 Otwinowski, Z. & Minor, W. Processing of X-ray diffraction data collected in oscillation mode. *Method Enzymol* **276**, 307-326 (1997).

31 Vagin, A. & Teplyakov, A. Molecular replacement with MOLREP. *Acta Crystallogr D Biol Crystallogr* **66**, 22-25 (2010).

32 Adams, P. D. *et al.* PHENIX: a comprehensive Python-based system for macromolecular structure solution. *Acta Crystallogr D Biol Crystallogr* **66**, 213-221 (2010).

33 Terwilliger, T. C. *et al.* Iterative model building, structure refinement and density modification with the PHENIX AutoBuild wizard. *Acta Crystallogr D Biol Crystallogr* **64**, 61-69 (2008).

34 Emsley, P. & Cowtan, K. Coot: model-building tools for molecular graphics. *Acta Crystallogr D Biol Crystallogr* **60**, 2126-2132 (2004).

35 Afonine, P. V., Grosse-Kunstleve, R. W. & Adams, P. D. in *CCP4 Newsl* Vol. 42 (2005).

36 Schuttelkopf, A. W. & van Aalten, D. M. PRODRG: a tool for high-throughput crystallography of protein-ligand complexes. *Acta Crystallogr D Biol Crystallogr* **60**, 1355-1363 (2004).

37 Laskowski, R. A., Macarthur, M. W., Moss, D. S. & Thornton, J. M. Procheck - a Program to Check the Stereochemical Quality of Protein Structures. *J Appl Crystallogr* **26**, 283-291 (1993).

38 Nicholls, A., Sharp, K. A. & Honig, B. Protein folding and association: insights from the interfacial and thermodynamic properties of hydrocarbons. *Proteins* **11**, 281-296 (1991).

39 Wallace, A. C., Laskowski, R. A. & Thornton, J. M. LIGPLOT: a program to generate schematic diagrams of protein-ligand interactions. *Protein Eng* **8**, 127-134 (1995).

40 Dundas, J. *et al.* CASTp: computed atlas of surface topography of proteins with structural and topographical mapping of functionally annotated residues. *Nucleic Acids Res* **34**, W116-118 (2006).

41 Krissinel, E. & Henrick, K. Secondary-structure matching (SSM), a new tool for fast protein structure alignment in three dimensions. *Acta Crystallogr D Biol Crystallogr* **60**, 2256-2268 (2004).

42 The PyMOL Molecular Graphics System (DeLano Scientific LLC, Palo Alto, CA, USA, 2008).

43 Wijesinghe, D. S. *et al.* Use of high performance liquid chromatography-electrospray ionization-tandem mass spectrometry for the analysis of ceramide-1-phosphate levels. *J Lipid Res* **51**, 641-651 (2010).

44 Hornick, J. E. *et al.* Amphiastral mitotic spindle assembly in vertebrate cells lacking centrosomes. *Current biology : CB* **21**, 598-605 (2011).

Table S1: Crystallographic data and refinement statistics for human CPTP complexes. Each crystal was obtained in a different crystal form having different packing interactions.

	Human CPTP/2:0-C1P	Human CPTP/8:0-C1P	Human CPTP/12:0-C1P	Human CPTP/16:0-C1P	Human CPTP/18:1-C1P	Human CPTP/12:0-PA
Data collection						
Space group	$P4_12_12$	$P2_12_12_1$	$P2_1$	$P2_1$	C2	$P2_12_12_1$
Unit cell a, b, c (Å) **α, β, γ (°)**	74.48, 74.48, 105.43 90, 90, 90	81.88,122.40 , 149.99 90, 90, 90	56.19, 132.68 , 62.11 90, 96.98, 90	62.60, 50.29, 62.87 90, 100.11, 90	236.98, 128.76, 66.66 90, 93.53, 90	46.91, 78.12, 107.71 90, 90, 90
Resolution[a] (Å)	50.0 -2.0 (2.07-2.0)	50.0 -3.2 (3.26-3.2)	50.0 -1.9 (1.97-1.9)	50.0 -1.9 (1.97-1.9)	30.0-3.1 (3.21-3.10)	50.0 -1.9 (1.97-1.9)
Total reflections	1425346	340890	1001212	519801	1505438	339238
Unique reflections	20690	25734	70898	30731	36056	32100
No of molecules/AU	1	6	4	2	6	2
Completeness (%)	99.9 (100.0)	99.8 (99.6)	99.1 (93.1)	99.7 (96.8)	99.3 (98.0)	99.5 (98.6)
$I/\sigma I$	32.65 (3.45)	19.6 (2.4)	22.2 (2.7)	31.4 (4.2)	18.1(2.6)	32.2 (3.3)
Redundancy	10.8 (11.0)	5.9 (5.8)	5.5 (4.7)	6.8 (4.5)	4.9 (5.0)	5.9 (5.9)
R_{merge}	8.2 (67.0)	8.6 (67.0)	7.2 (44.0)	7.9 (26.9)	11.0 (47.8)	5.8 (45.9)
Refinement						
R_{work} / R_{free}	17.2/22.1	22.2/26.5	18.3/23.1	16.2/21.3	22.9/26.9	18.9/23.5
RMSD **Bond lengths (Å)** **Bond angles (°)**	 0.007 0.929	 0.006 0.997	 0.007 1.041	 0.007 0.936	 0.006 1.059	 0.005 0.924
No. of atoms **Protein/Lipid/H_2O**	1664/28/234	9757/149/9	6665/152/684	3339/84/439	9865/219/16	3319/72/276
Average B-factors (Å^2) **Protein/Lipid/ H_2O**	31.1/30.5/39.8	81.7/54.5/44.8	29.3/31.7/36.4	21.1/29.0/30.8	89.8/76.5/46.6	32.3/30.6/39.8
Ramachandran statistics (%) **mostly allowed** **allowed** **generously allowed** **disallowed regions**	 93.7 6.3 0.5 0.0	 92.6 7.4 0.0 0.0	 94.2 5.8 0.0 0.0	 93.6 6.4 0.0 0.0	 86.5 13.5 0.0 0.0	 93.1 6.9 0.0 0.0

[a]Values for highest resolution shell are shown in parentheses.

Table S2: Crystallographic statistics for Seleno-methionine (Se-Met) labelled human CPTP in complex with 8:0-C1P and mouse CPTP in apo-form.

	Se-Met human CPTP/8:0-C1P	**Mouse CPTP in apo-form**
Data collection		
Wavelength (Å)	0.9790 (Se-Peak)	0.9792
Space group	$P2_12_12_1$	$P2_12_12_1$
Unit cell a, b, c (Å) α, β, γ (°)	81.51,121.73, 150.58 90, 90, 90	82.00, 83.88, 268.72 90, 90, 90
Resolution[a] (Å)	50.0 -3.3 (3.42-3.3)	50-2.55 (2.64-2.55)
Total reflections	570839	1278880
Unique reflections	23560	61660
No of molecules/AU	6	8
Completeness (%)	98.2 (90.7)	93.5 (83.4)
$I/\sigma I$	14.4 (2.7)	25.5 (3.2)
Redundancy	4.6 (2.7)	10.0 (10.6)
R_{merge}	8.7 (27.2)	8.6 (59.6)
Se-SAD phasing		
Resolution (Å)	50.0 -3.3	
No. of Se atoms	24 (out of possible 30)	
Figure of merit (FOM) Overall FOM Overall FOM (after density modification)	 0.40 0.73	
Refinement		
R_{work} / R_{free}		20.1/27.1
RMSD Bond lengths (Å) Bond angles (°)		 0.009 1.151
No. of atoms Protein/Water		 12910/254
Average B-factors (Å^2) Protein/Water		 55.5/47.4
Ramachandran statistics (%) mostly allowed regions allowed regions generously allowed regions disallowed regions		 90.9 9.1 0.0 0.0

[a]Values for highest resolution shell are shown in parentheses.

Table S3. Crystallization conditions for human CPTP complexes and for apo-form of mouse CPTP.

Crystals*	**Crystallization condition**
Human CPTP/2:0-C1P	0.2 M Ammonium acetate, 0.1 M HEPES pH 7.5, 25% PEG3,350
Human CPTP/8:0-C1P	0.2 M Ammonium sulfate, 0.1 M Tris pH 8.0, 20% PEG3,350
Human CPTP/12:0-C1P	0.2 M Ammonium chloride, 0.1 M Hepes pH 7.0, 20% PEG6,000
Human CPTP/16:0-C1P	0.1 M MMT buffer[#] pH 5.0, 25% PEG1,500
Human CPTP/18:1-C1P	0.2 M Sodium malonate, 0.1 M Bis-Tris Propane pH 6.5, 20% PEG3,350
Human CPTP/di12:0-PA	0.2 M Sodium acetate, 0.1 M Bis-Tris propane pH 6.5, 20% PEG3,350
Se-Met Human CPTP/8:0-C1P	0.2 M Sodium Acetate trihydrate, 20% PEG3,350
Mouse CPTP in apo-form	0.1 M Bis-Tris pH 6.5, 2 M Ammonium sulfate

[#] MMT buffer is produced by mixing DL-malic acid, MES and Tris base in the molar ratios 1:2:2 – DL-malic acid: MES: Tris base.

* Each crystal was obtained in a different crystal form having different packing interactions.

Table S4. Solvent-accessible volume and area calculated for hydrophobic tunnel in CPTP structures using the program CASTp.

	Solvent-accessible volume (Å^3)	Solvent-accessible area (Å^2)
Mouse CPTP in apo-form		
Mouse CPTP	39.8	86.5
Human CPTP complexes in sphingosine-out conformation		
8:0-C1P/CPTP	104.3	198.01
12:0-C1P/CPTP	260.9	364.72
di12:0-PA/CPTP	110.2	220.65
Human CPTP complexes with sphingosine-in conformation		
2:0-C1P/CPTP	263.0	363.4
12:0-C1P/CPTP	329.2	522.9
16:0-C1P/CPTP	363.7	529.4
18:1-C1P/CPTP	387.0	602.8

Table S5: Precursor and product ion pairs used in the quantitative analysis of sphingolipids and eicosanoids via multiple reaction monitoring (MRM).

Sphingolipids

Species	Precursor ion (*m/z*)	Product ion (*m/z*)
$d_{18:1/12:0}$ C1P	562.4	264.4
$d_{18:1/14:0}$ C1P	590.4	264.4
$d_{18:1/16:0}$ C1P	618.5	264.4
$d_{18:0/16:0}$ C1P	620.5	266.4
$d_{18:1/18:1}$ C1P	644.5	264.4
$d_{18:1/18:0}$ C1P	646.5	264.4
$d_{18:1/20:0}$ C1P	674.4	264.4
$d_{18:1/22:0}$ C1P	702.7	264.4
$d_{18:1/24:1}$ C1P	728.6	264.4
$d_{18:1/24:0}$ C1P	730.6	264.4
$d_{18:1/26:1}$ C1P	756.7	264.4
$d_{18:1/26:0}$ C1P	758.7	264.4
$d_{18:1/12:0}$ Cer	482.6	264.4
$d_{18:1/14:0}$ Cer	510.7	264.4
$d_{18:1/16:0}$ Cer	538.7	264.4
$d_{18:0/16:0}$ Cer	540.7	266.4
$d_{18:1/18:1}$ Cer	564.7	264.4
$d_{18:1/18:0}$ Cer	566.7	264.4
$d_{18:1/20:0}$ Cer	594.7	264.4
$d_{18:1/22:0}$ Cer	622.8	264.4
$d_{18:1/24:1}$ Cer	648.9	264.4
$d_{18:1/24:0}$ Cer	650.9	264.4
$d_{18:1/26:1}$ Cer	676.9	264.4
$d_{18:1/26:0}$ Cer	678.9	264.4
$d_{18:1/12:0}$ Monohex-Cer	644.6	264.4
$d_{18:1/14:0}$ Monohex-Cer	672.6	264.4
$d_{18:1/16:0}$ Monohex-Cer	700.7	264.4
$d_{18:0/16:0}$ Monohex-Cer	702.5	266.4
$d_{18:1/18:1}$ Monohex-Cer	728.7	264.4
$d_{18:1/18:0}$ Monohex-Cer	730.7	264.4
$d_{18:1/20:0}$ Monohex-Cer	756.7	264.4
$d_{18:1/22:0}$ Monohex-Cer	784.8	264.4
$d_{18:1/24:1}$ Monohex-Cer	810.9	264.4
$d_{18:1/24:0}$ Monohex-Cer	812.9	264.4
$d_{18:1/26:1}$ Monohex-Cer	838.9	264.4
$d_{18:1/26:0}$ Monohex-Cer	840.9	264.4
$d_{18:1/12:0}$ SM	647.7	184.4
$d_{18:1/14:0}$ SM	675.7	184.4
$d_{18:1/16:0}$ SM	703.8	184.4
$d_{18:0/16:0}$ SM	705.8	184.4
$d_{18:1/18:1}$ SM	729.8	184.4
$d_{18:1/18:0}$ SM	731.8	184.4
$d_{18:1/20:0}$ SM	759.9	184.4
$d_{18:1/22:0}$ SM	787.9	184.4
$d_{18:1/24:1}$ SM	813.9	184.4
$d_{18:1/24:0}$ SM	815.9	184.4
$d_{18:1/26:1}$ SM	841.9	184.4
$d_{18:1/26:0}$ SM	843.9	184.4

Eicosanoids

Species	Precursor ion (m/z)	Product ion (*m/z*)
$PGF_2\alpha$	353	193
$PGF_2\alpha$-d_4	357	197
PGE_2	351	271
PGE_2-d_4	355	275
PGD_2	351	271
PGD_2-d_4	355	275
LTB_4	335	195
LTE_4	438	235
6-keto $PGF_1\alpha$	369	163
6-keto $PGF_1\alpha$-d_4	373	167
PGI_2	351	214
PGJ_2	333	233
5 HETE	319	115
5 HETE-d_8	327	116
8 HETE	319	155
11 HETE	319	167
12 HETE	319	179
11,12 EET	319	167
Arachidonic Acid	303	259
Arachidonic Acid-d_8	311	267

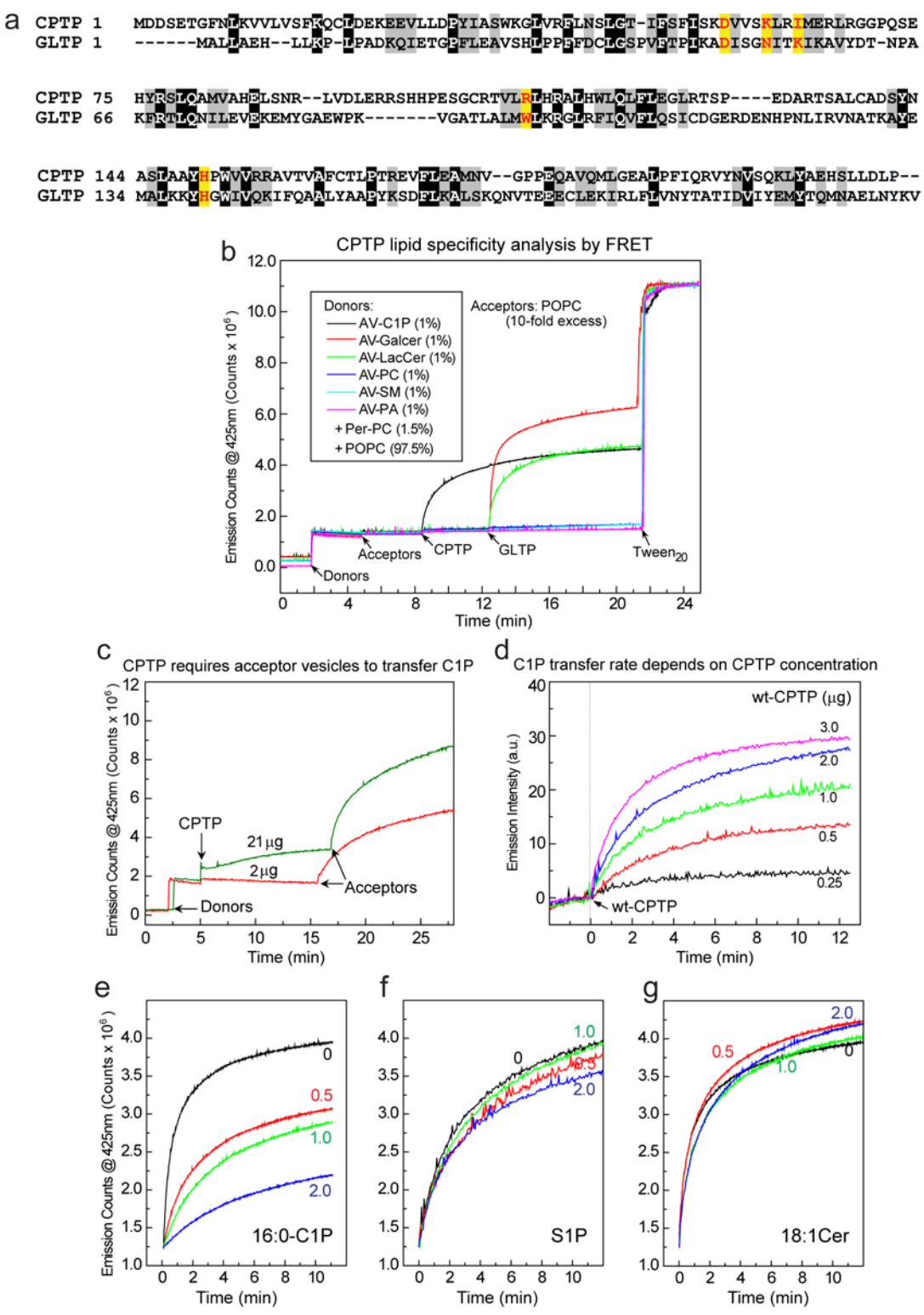

Figure S1. Human CPTP and GLTP sequences and CPTP fluorescent lipid transfer between membranes. a, Sequence alignment of human CPTP and human GLTP. Conserved residues interacting with lipid head group are red with yellow highlights. **b,** Transfer of AV-labeled lipids by CPTP (2 µg) as a function of time. The exponential increase in fluorescence emission at 425 nm (AV emission) occurs

because of AV-lipid removal from donor vesicles (that also contain 3-perylenoyl-PC; Förster resonance energy transfer receiver) and transport to POPC acceptor vesicles. AV-C1P is the only lipid transferred by CPTP. Addition of GLTP results in immediate transfer of AV-GalCer or AV-LacCer which is inert to CPTP. **c,** CPTP functions as a C1P transfer protein. Addition of catalytic amounts CPTP (0.5-2 μg) in the absence of acceptor vesicles results in no change in signal response, while large CPTP amounts cause a trace of signal change. Acceptor vesicle addition induces immediate and rapid AV-C1P transfer. **d,** The initial rate of C1P transfer depends on the protein concentration of CPTP. **e,** Competition effect by 16:0-C1P on AV-C1P transfer by CPTP. Inclusion of 16:0-C1P [0.5 mole% (red), 1 mole% (green), or 2 mole% (blue)] in the donor vesicles along with AV-C1P strongly diminished the transfer rates of AV-C1P. **f,** Competition effect by sphingosine-1-phosphate (S1P) on AV-C1P transfer by CPTP. Inclusion of S1P [0.5 mole% (red), 1 mole% (green), or 2 mole% (blue)] in the donor vesicles along with AV-C1P (1 mole%) results in almost no slow-down in the transfer rates of fluorescent C1P. **g,** Competition effect by 18:1-ceramide (Cer) on AV-C1P transfer by CPTP. Inclusion of Cer [0.5 mole% (red), 1 mole% (green), or 2 mole% (blue)] in the donor vesicles along with AV-C1P (1 mole%) has almost no effect on the transfer rate of fluorescent C1P.

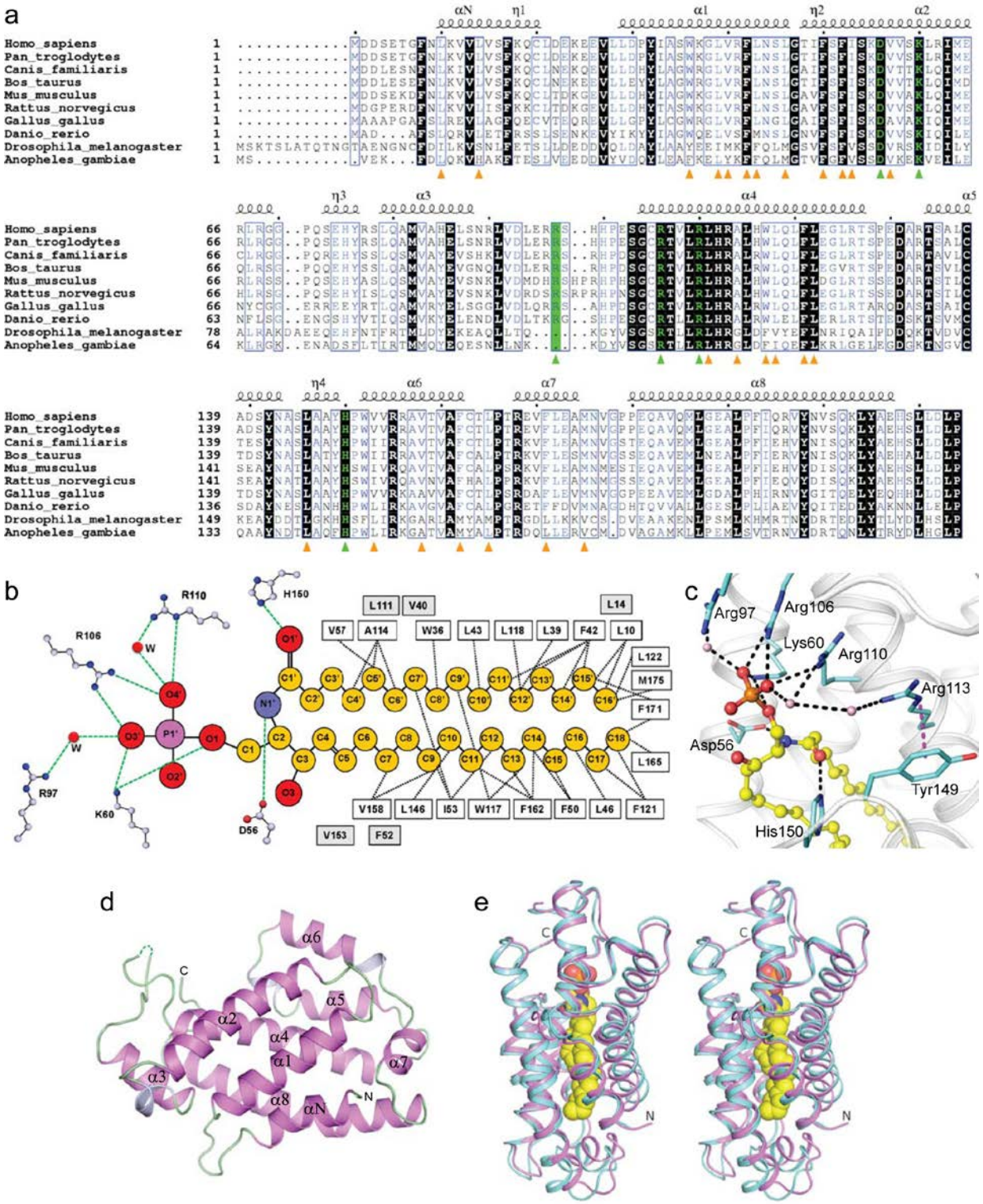

Figure S2. Sequence alignment of CPTP homologs from different organisms, schematic representation of intermolecular contacts for 16:0-C1P recognition by human CPTP in the sphingosine-in mode, and the overall structure of mouse CPTP in apo-form. **a,** Amino acid sequence alignment between CPTP homolog's from various organisms. Human CPTP residues interacting with head group of C1P are highlighted in green and shown by green triangles below the aligned sequences.

Orange triangles indicate human CPTP residues involved in formation of hydrophobic tunnel. The secondary structure elements of 16:0-C1P bound human CPTP are represented at the top of the aligned sequences by spirals (α-helices and 3_{10} helices). α-helices (αN and α1-α8) and 3_{10} helices (η1-η4) are numbered from the N- to the C-terminus. NCBI references sequence number along with length of amino acids for CPTP and its homologous sequences are given below: *Homo sapiens* (NP_001025056.1, 214 aa), *Pan troglodytes* (XP_524838.1, 214 aa), *Canis lupus familiaris* (XP_546715.1, 214 aa), *Bos taurus* (NP_001068650.1, 214 aa), *Mus musculus* (NP_077792.2, 216 aa), *Rattus norvegicus* (NP_001007704.1, 216 aa), *Gallus gallus* (XP_417578.1, 214 aa), *Danio rerio* (XP_001330928.1, 211 aa), *Drosophila melanogaster* (NP_611572.2, 223 aa) and *Anopheles gambiae* (XP_316032.4, 207 aa). **b,** The schematic shows intermolecular contacts for 16:0-C1P in a sphingosine-in conformation with CPTP. Carbon, oxygen, nitrogen and phosphorous atoms of 16:0-C1P are shown as spheres colored yellow, red, blue and magenta, respectively. Residues interacting with lipid headgroup are shown with carbon atoms colored silver. Water molecules are shown as small red spheres. Residues forming the hydrophobic pocket are shown as black rectangular boxes. Green dashed lines show the hydrogen bonds, whereas black dotted lines indicate hydrophobic interaction between CPTP residues and nonpolar 16:0-C1P chains. Residues shown in black boxes with gray background are involved in hydrophobic pocket formation. **c,** CPTP lipid headgroup recognition centre residues interacting with the phosphate moiety and the amide group of bound 16:0-C1P. The cation-pi interaction between Arg113 and Tyr149 is shown by the red dashed line. Hydrogen bonds are shown by dashed black lines. The CPTP Cα backbone is colored light gray and the side chain carbon atoms are shown in cyan, and oxygen and nitrogen atoms are shown in red and blue, respectively. 16:0-C1P is shown in ball-and-stick representation and water molecules are shown as pink spheres. **d,** Crystal structure of mouse CPTP in apo-form with α-helices (colored violet), 3_{10}-helices (colored light gray) and loop regions (colored light green) shown in ribbon representations. α-helices (αN and α1-α8) are numbered from the N- to the C-terminus. **e,** Stereo view of the structural superposition between mouse CPTP in apo-form and human CPTP in complex with 16:0-C1P. Mouse CPTP (violet) and human CPTP (cyan) are shown in ribbon representation whereas 16:0-C1P (yellow) bound to human CPTP is shown in a space-filling representation.

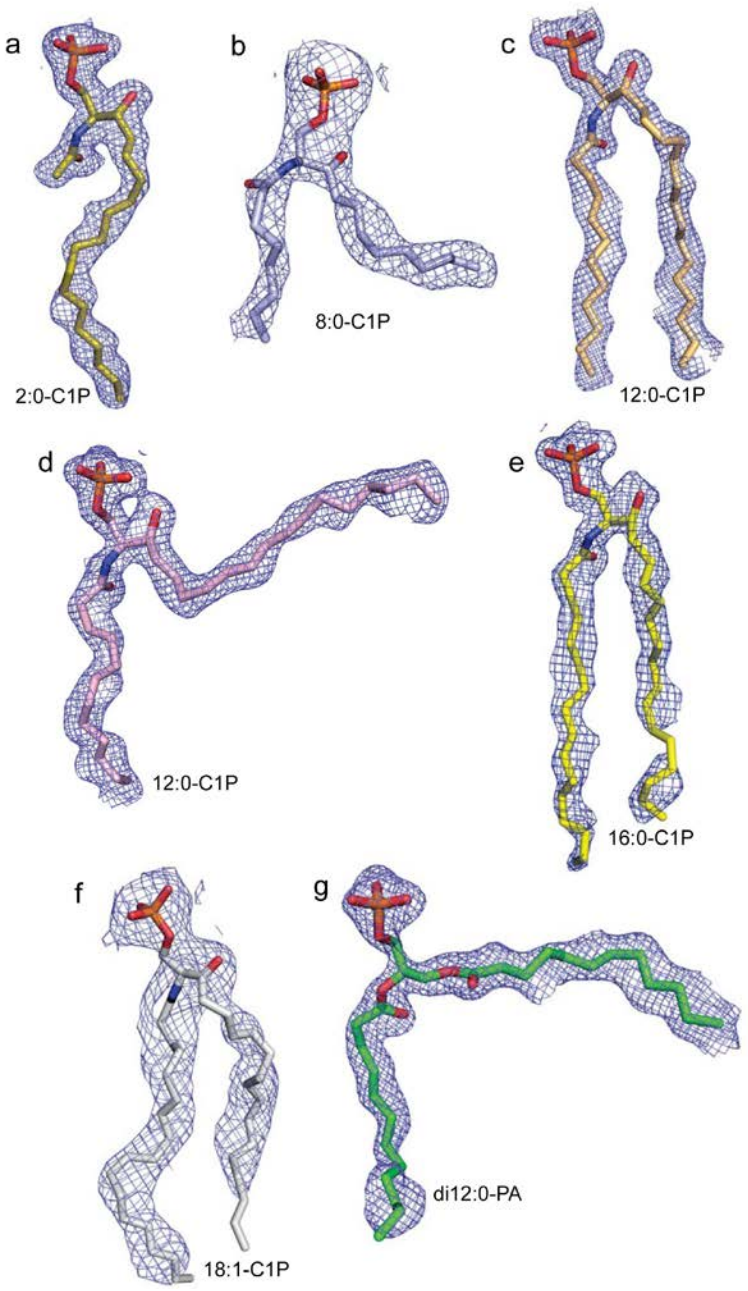

Figure S3. **Omit map (*2Fo-Fc*) contoured at 1σ level for ligands bound to CPTP in the complexes**. **a,** Omit map (2.0 Å resolution) for 2:0-C1P in the sphingosine-in arrangement involving CPTP. **b,** Omit map (3.2 Å resolution) for 8:0-C1P in the sphingosine-out arrangement involving CPTP. The last eight carbon atoms of the sphingosine chain were not built due to the lack of electron density. **c,** Omit map (1.9 Å resolution) for 12:0-C1P in the sphingosine-in arrangement involving CPTP. **d,** Omit map (1.9 Å resolution) for 12:0-C1P in the sphingosine-out arrangement involving CPTP. **e,** Omit map (1.9 Å resolution) for 16:0-C1P in the 'sphingosine-in' arrangement involving CPTP. **f,** Omit map (3.1 Å resolution) at 1σ level for 18:1-C1P in the sphingosine-in arrangement involving CPTP. **g,** Omit map (1.9 Å resolution) for di12:0-PA in the sphingosine-out like arrangement involving CPTP.

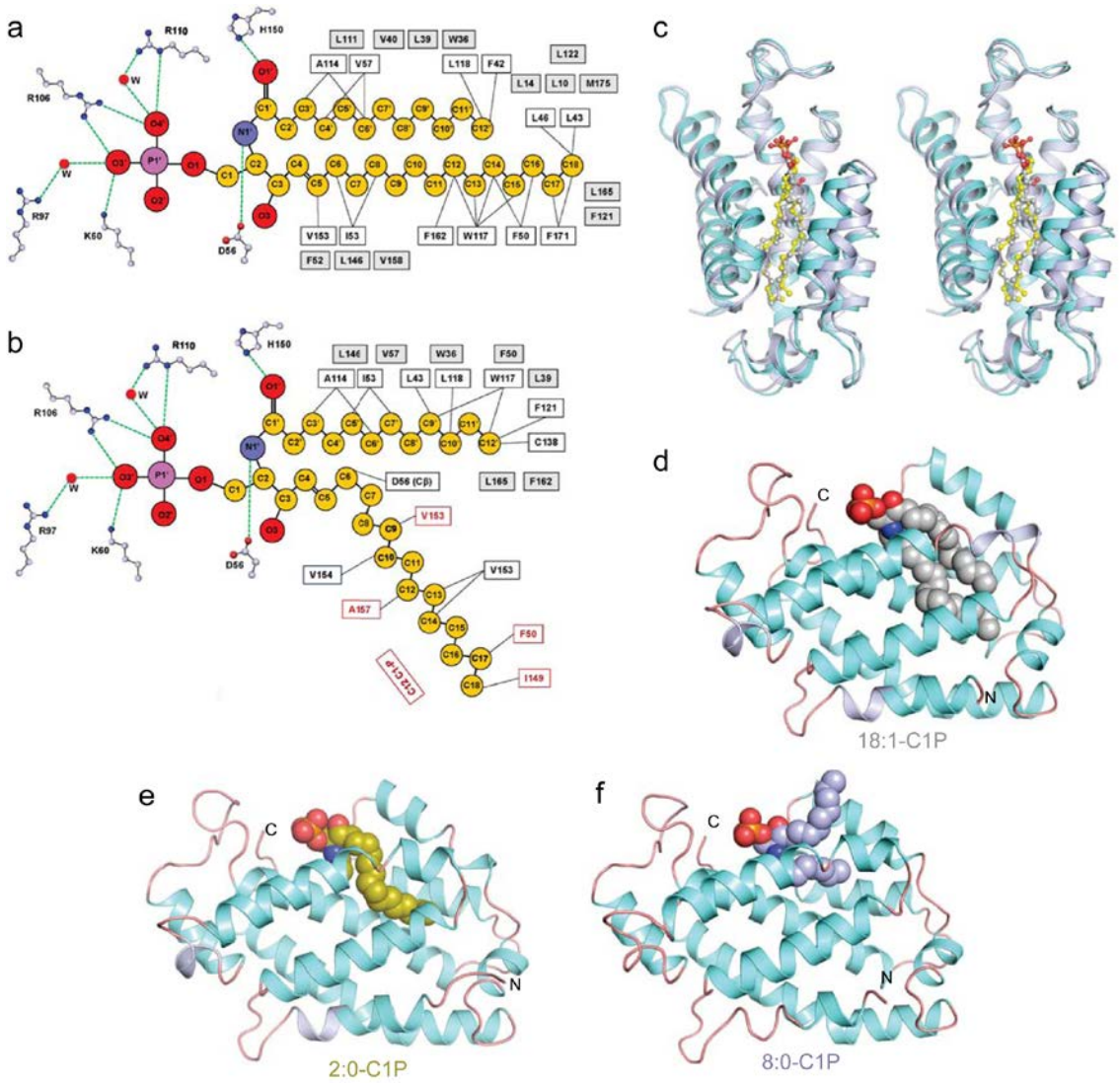

Figure S4. Schematic representations of inter-molecular contacts involving 12:0-C1P recognition by human CPTP in sphingosine-in and sphingosine-out modes and crystal structures of human CPTP in complex with 2:0-C1P, 18:1-C1P and 8:0-C1P. **a, b,** The upper schematic shows intermolecular contacts for 12:0-C1P in sphingosine-in conformation with CPTP (panel a), whereas the lower panel shows related intermolecular contacts for 12:0-C1P in sphingosine-out conformation with CPTP (panel b). The figures are drawn in the same way as Supplementary Figure S2b. The residues shown in brown rectangular boxes are from symmetry related molecule. Both binding modes are observed in the same asymmetric unit with two molecules each in the sphingosine-in (panel a) and -out modes (panel b) enabling comparison under the closest possible conditions. **c,** Stereo view showing structural superposition of human CPTP (cyan) in complex with 18:1-C1P (carbon atoms in silver) and human CPTP (blue) in complex with 16:0-C1P (carbon atoms in silver). Lipid molecules are shown in ball and stick representation. **d,** Crystal structure of CPTP (ribbon representation) in complex with 18:1-C1P (space-filling representation, silver). **e,** Crystal structure of CPTP (ribbon representation) in complex with 2:0-C1P (space-filling representation, olive). **f,** Crystal structure of CPTP (ribbon representation) in complex with 8:0-C1P (space-filling representation, blue). The electron density of the last six-methylene groups in the sphingosine chain was disordered.

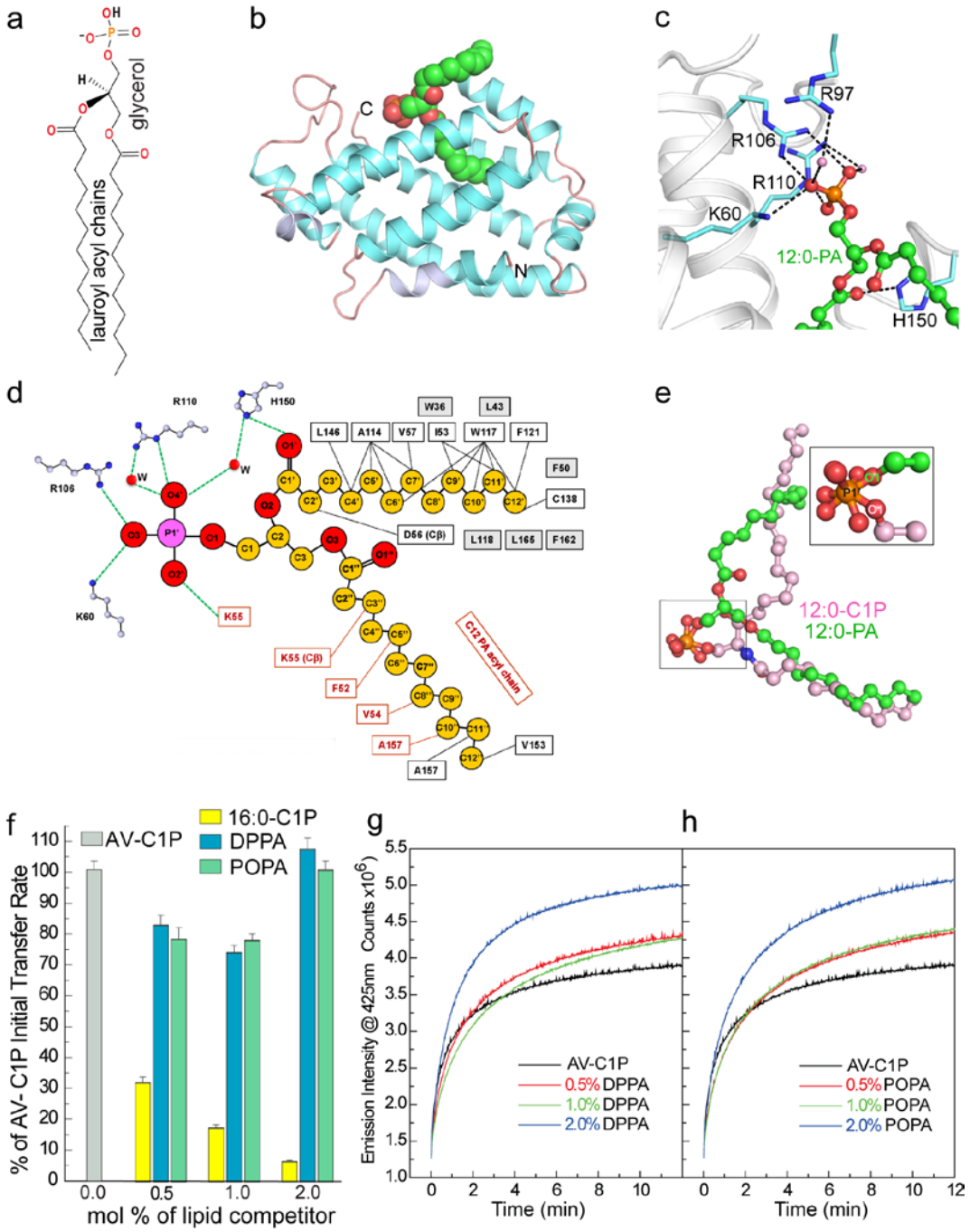

Figure S5. Nonproductive binding interaction between CPTP and PA. **a,** Chemical formula of di-dodecanoyl-phosphatidic acid (di12:0-PA). **b,** Crystal structures of human CPTP (ribbon representation) in complex with di12:0-PA (green, space-filling representation) in 'sphingosine-out like' conformation. **c,** Hydrogen bond network between human CPTP residues and head group of di12:0-PA. Color-coding is same as in Figure 2a. **d,** Schematic showing intermolecular contacts for di12:0-PA in the sphingosine-out like conformation with CPTP. The figure is drawn in the same way as Supplementary Figure S2b. The residues shown in brown rectangular boxes are from symmetry related molecule. **e,** Superposition of stick representations of bound di12:0-PA (carbon atoms in green) and bound 12:0-C1P (carbon atoms in pink) in sphingosine-out conformations of respective CPTP complexes. Inset shows conformational differences

of the bound lipid headgroups. **f,** Summary of competition effects exerted by 16:0-C1P, DPPA, and POPA on the CPTP-mediated initial transfer rate of fluorescent C1P. Data represent the mean ± s.d. of three independent experiments. **g, h,** Functional analysis shows nonfluorescent PA to be an ineffective competitor against AV-C1P transfer by CPTP. Panel g shows that increasing amounts of dipalmitoyl phosphatidic acid (DPPA) exert no competition effect on the CPTP-mediated transfer of fluorescent C1P. DPPA amounts in the donor vesicles with AV-C1P (1 mole%) are 0.5 mole% (red); 1 mole% (green); 2 mole% (blue). Panel h shows that increasing amounts of 1-palmitoyl-2-oleoyl phosphatidic acid (POPA) also exert no competition effect on the CPTP-mediated transfer of fluorescent C1P. POPA amounts are 0.5 mole% (red); 1 mole% (green); 2 mole% (blue).

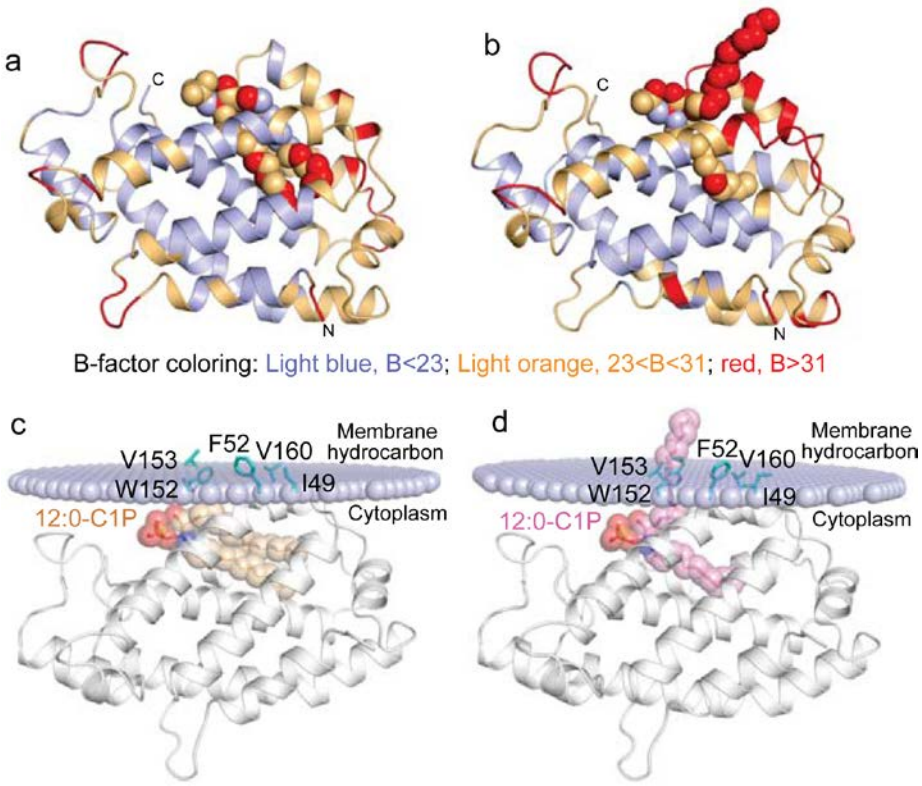

Figure S6. CPTP conformational flexibility associated with sphingosine-in and -out binding modes of C1P and models of C1P-bound CPTP interaction with the membrane. a, b, B-factor distribution of human CPTP/12:0-C1P complexes in sphingosine-in (panel a) and sphingosine-out (panel b) conformations. Human CPTP is shown in ribbon representation, and bound 12:0-C1P is shown in space-filling representation. **c, d,** The OPM computational approach was used to calculate the probable position of sphingosine-in and -out conformation of 12:0-C1P bound CPTP with respect to the hydrocarbon core of the lipid bilayer. C1P bound CPTP is shown in light gray whereas residues that penetrate into the membrane hydrocarbon region are shown in cyan. 12:0-C1P is shown in wheat for sphingosine-in (panel c) and in pink for sphingosine-out (panel d) conformations. Lavender colored spheres show the boundary of membrane hydrocarbon. Headgroups of membrane lipids are expected to project approximately 10 Å beyond towards the protein molecule.

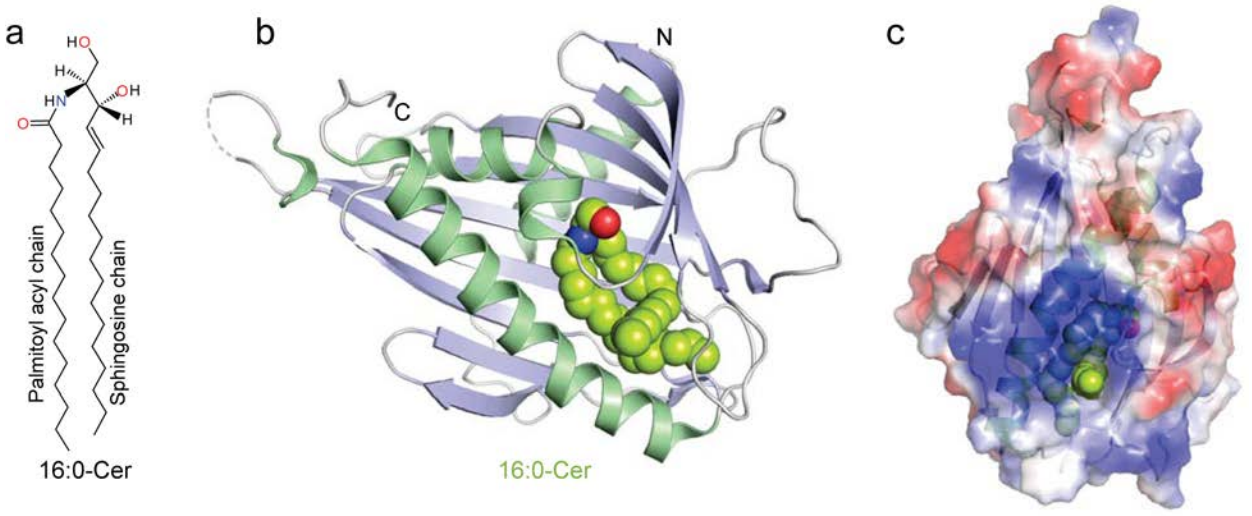

Figure S7. Overall structure of the START domain of ceramide transfer protein (CERT) domain in complex with N-palmitoyl-ceramide (16:0-Cer). **a,** Chemical formula of 16:0-Cer. **b,** Crystal structure of START domain of CERT in complex with 16:0-Cer (PDB code: 2E3O). α-helices (colored light green), β-strands (colored light blue) and loop regions (colored light gray) are shown in ribbon representations and bound ceramide is shown in a space-filling representation with carbon atoms colored in green whereas oxygen and nitrogen atoms are colored in red and blue, respectively. **c,** Electrostatic surface view and ribbon representation of START domain of CERT bound to 16:0-Cer in a space-filling representation.

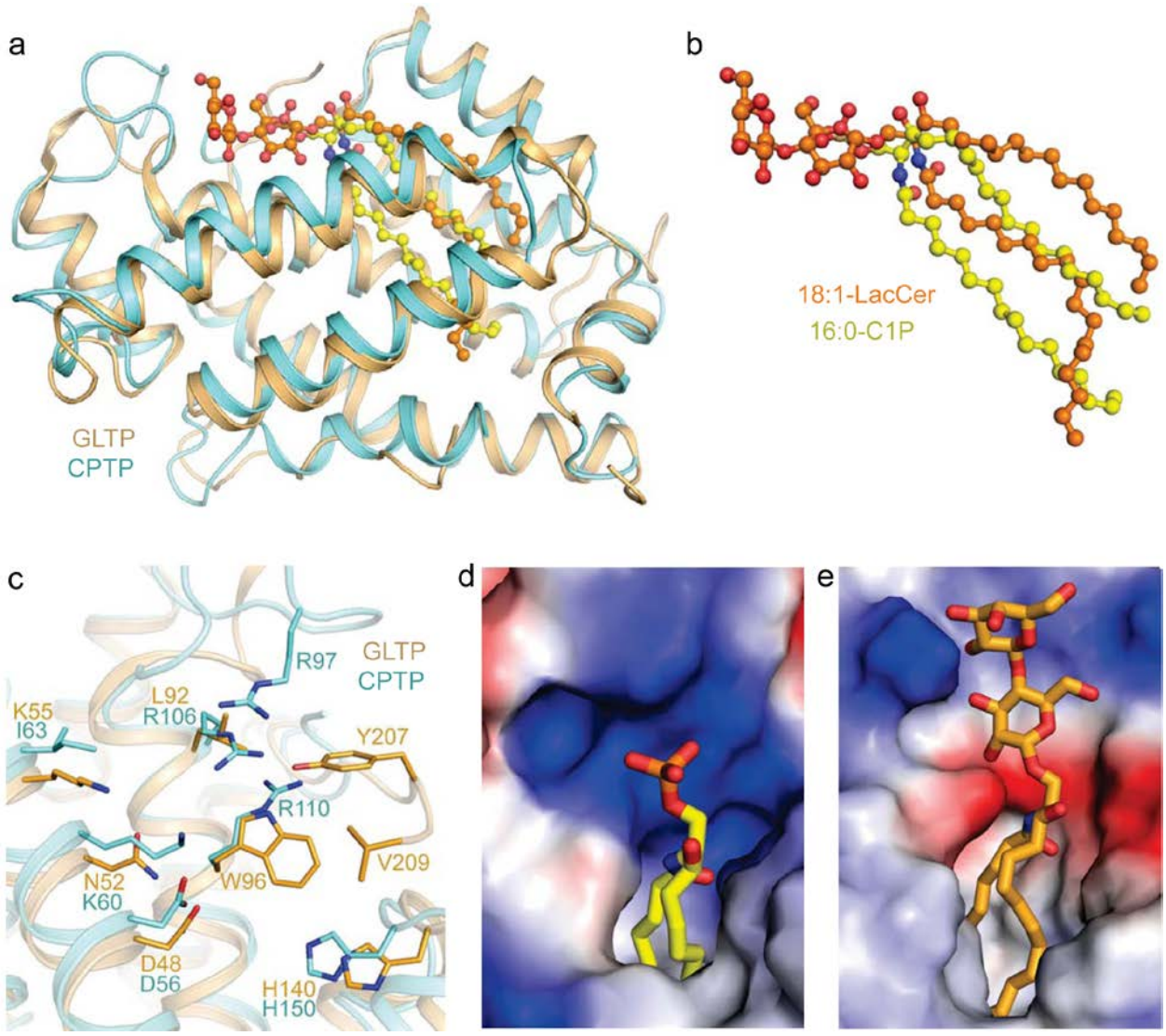

Figure S8. Structural comparison of 16:0-C1P bound to human CPTP and 18:1-LacCer bound to human GLTP complexes. **a,** Structural superposition of human CPTP (cyan) in complex with 16:0-C1P (carbon atoms in yellow) and human GLTP (light orange) in complex with 18:1-LacCer (carbon atoms in orange). Lipid molecules are shown in ball and stick representation. **b,** Relative positioning of bound 16:0-C1P (carbon atoms in yellow) and bound 18:1-LacCer (carbon atoms in orange) from the superposed structures of complexes. **c,** Structural superposition of amino acid residues involved in lipid head-group recognition in human CPTP (carbon atoms in cyan) and GLTP (carbon atoms in orange) structures of complexes. Side chain atoms of amino acids are shown in stick representation. **d, e,** Electrostatic surface views of lipid head group-binding pockets in human CPTP bound to C1P (panel d) and human GLTP bound to LacCer (panel e). C1P and LacCer molecules are shown in stick representation and colored yellow (panel d) and orange (panel e), respectively.

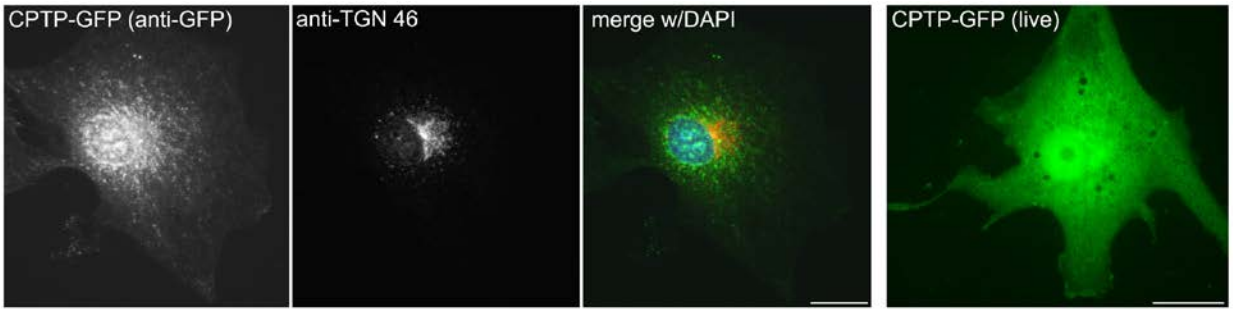

Figure S9. CPTP-GFP intracellular localization. CPTP-GFP localizes to the Golgi region (as judged by anti-TGN46 labeling), nucleus and plasma membrane in cultured mammalian cells expressing EGFP-CPTP. The nuclear localization of EGFP-CPTP in fixed cells mirrors the localization in live cells. Bar = 10 μm.

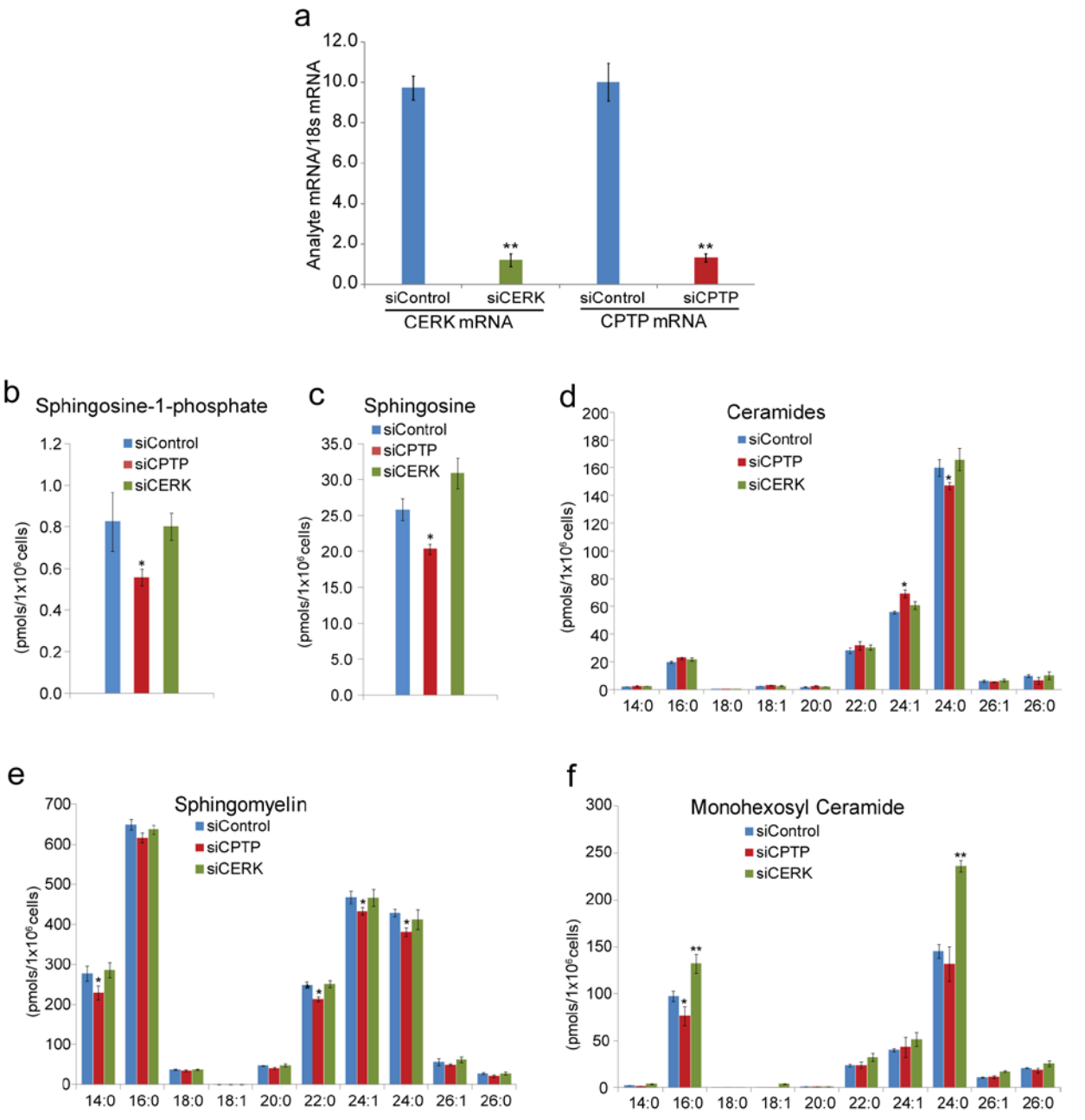

Figure S10. Effects of siRNA-mediated downregulation of CERK and of CPTP on sphingolipid metabolites. Intracellular sphingolipid levels are expressed in units of picomols per million cells. **a,** efficiency of siRNA knockdown of CERK and CPTP compared to non-specific controls. **b, c,** sphingosine-1-phosphate (S1P) and sphingosine expressed. **d,** ceramide. **e,** sphingomyelin. **f,** monohexosyl ceramide. For Cer (**d**), sphingomyelin (**e**), and monohexosyl ceramide (**f**), x-axis labels represent the acyl composition linked to sphingosine base chain ($d_{18:1}$). Data represent the average of 6 experiments from 2 separate procedures with Student's t-test used to assess statistical significance (* $p<0.05$, ** $p<0.01$, NS not significant). See on-line Methods and Supplementary Methods for details of protocols.

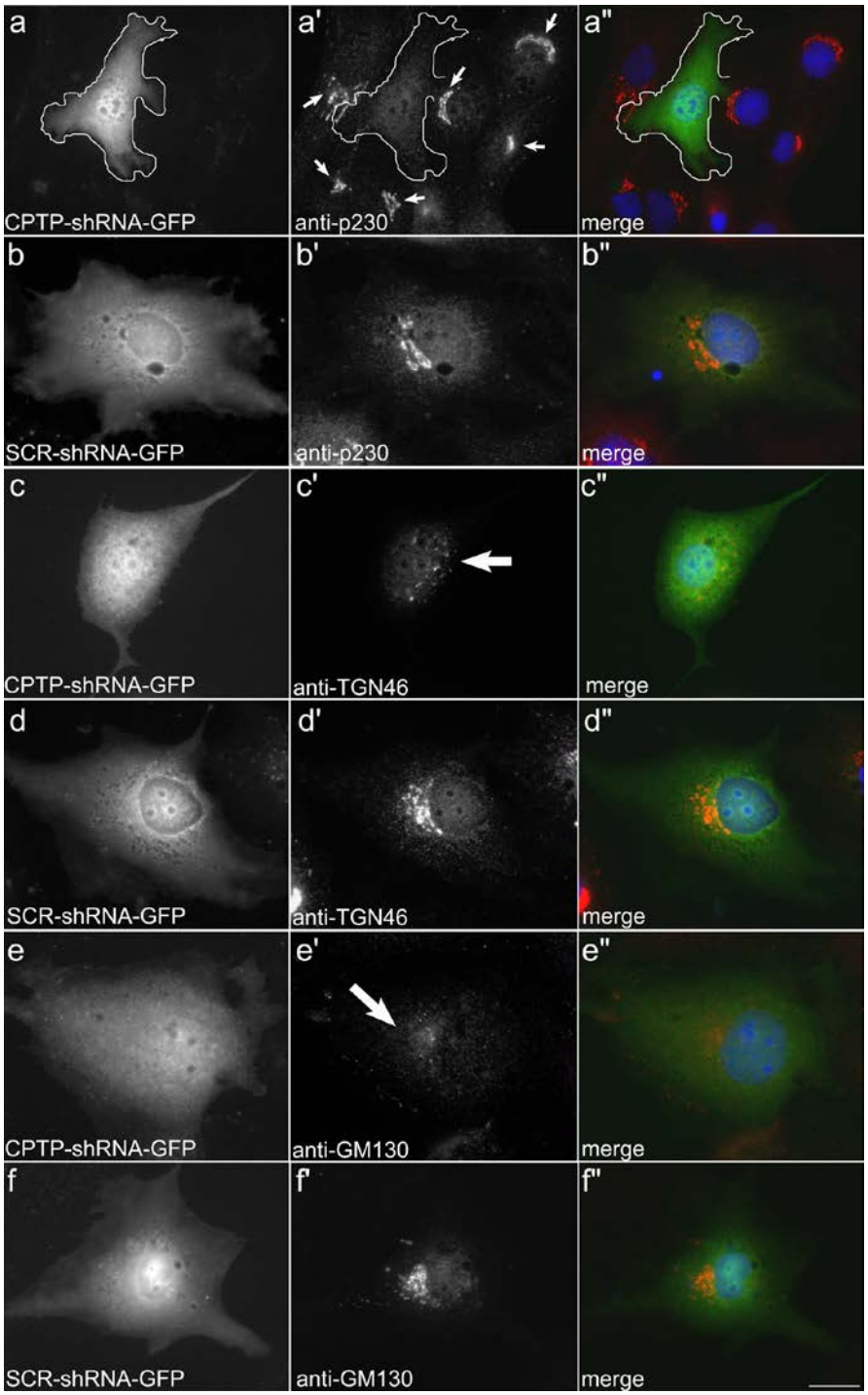

Figure S11. Knock-down of CPTP induces disappearance of Golgi stacks via vesiculation. a-a", BSC1 cell expressing an shRNA-GFP plasmid encoding a hairpin targeting CPTP lacks Golgi cisternae (determined by antip230 labeling), compared to adjacent non-transfected cells (position of Golgi marked by arrows). **b-b"**, Control cell, transfected with shRNA-GFP plasmid encoding a scrambled hairpin – this cell retains its p230 positive organized Golgi apparatus. Knockdown of CPTP disrupts Golgi stacks (arrows) labeled with anti-TGN 46 (**c-c"**) and anti-GM 130 (**e-e"**). **d-d"**, and **f-f"**, scrambled controls have intact Golgi cisternae. Bar = 10 μm.

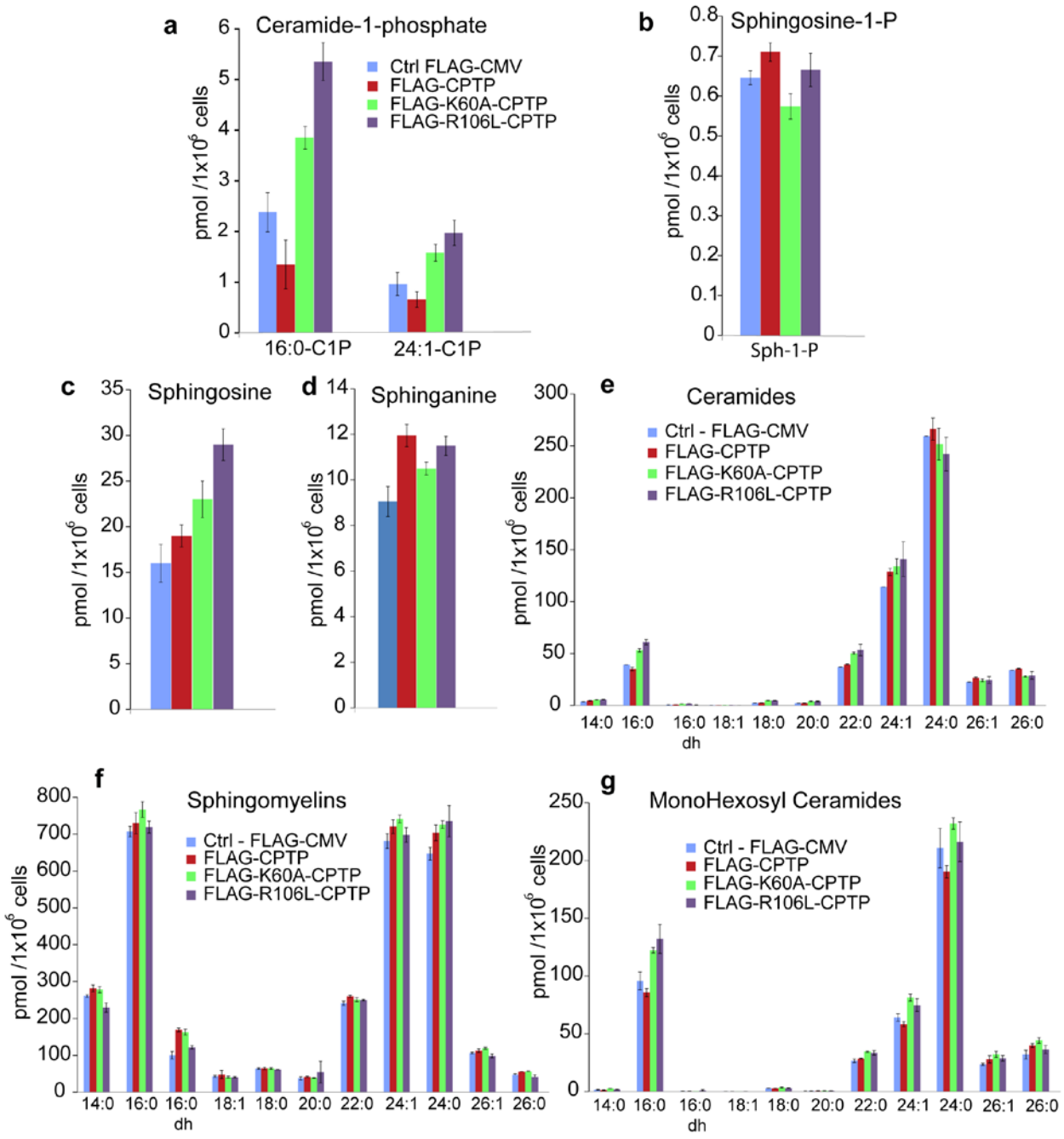

Figure S12. Effect of CPTP and mutant CPTP ectopic expression on cellular sphingolipid levels. Intracellular sphingolipid levels are expressed in units of picomoles per million cells. **a,** ceramide-1-phosphate (C1P). **b, c, d,** sphingosine-1-phosphate (S1P), sphingosine ($d_{18:1}$), and sphinganine ($d_{18:0}$). **e,** ceramide. **f,** sphingomyelin. **g,** monohexosyl ceramide. For Cer (**e**), sphingomyelin (**f**), and monohexosyl ceramide (**g**), x-axis labels represent the acyl composition linked to sphingosine base chain ($d_{18:1}$). Data represent the mean ± s.d. of three independent experiments. (See on-line Methods and Supplementary Methods).

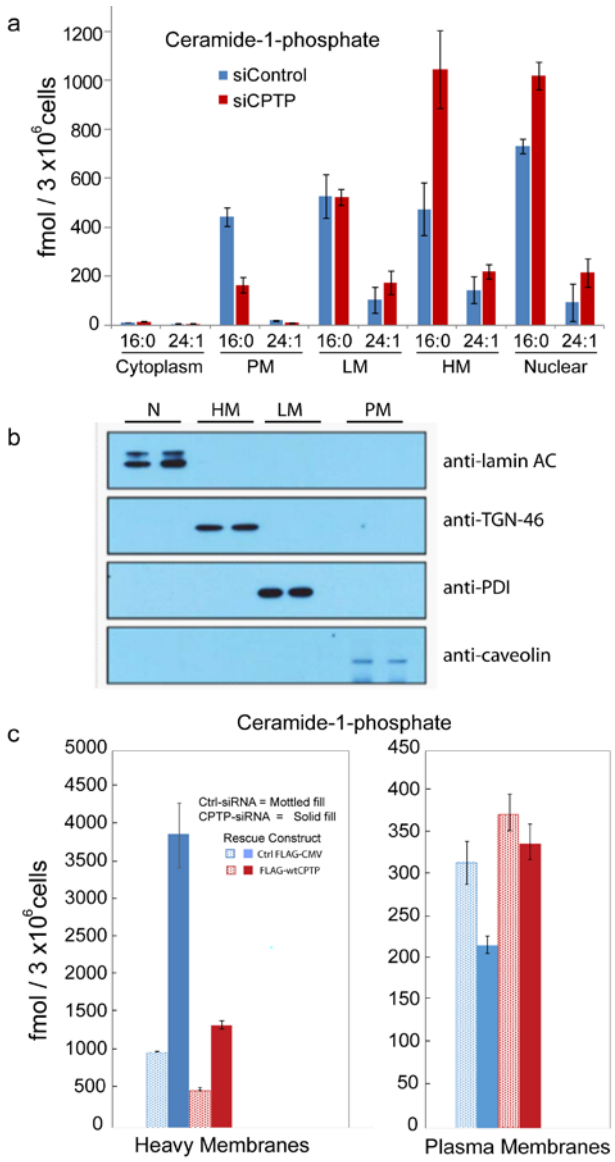

Figure S13. Subcellular sites where RNAi-induced CPTP depletion affects C1P levels. a, Subcellular fractions obtained by centrifugation of control and siRNA-CPTP-treated A549 cells were assessed for C1P content by HPLC-ESI/MS analyses detailed in the Methods. Data represent the mean ± s.d. of three independent experiments. **b,** SDS-PAGE/Western blotting validation of subcellular fraction enrichment using organelle markers anti-lamin AC for nucleus, anti-TGN46 for *trans*-Golgi, anti-protein disulfide isomerase (PDI) for ER, and anti-caveolin 1 for plasma membrane. Details of centrifugal separations appear in the Supplementary Methods. For each subcellular fraction, the first lane shows control cells and the second lane shows siRNA-CPTP-treated cells. NM, nuclear membranes; LM, light membranes are ER-/*cis*-Golgi-enriched; HM, heavy membranes are *trans*-Golgi-/endosome-/mitochondria-enriched; PM, plasma membrane. **c,**Rescue effect exerted by ectopic expression of wtCPTP on C1P levels in endomembranes and plasma membranes subfractionated by centrifugation as described in the Supplementary Methods. Data represent the mean ± s.d. of three independent experiments. SM levels in these same membrane fractions are unaffected by siRNA-induced CPTP depletion compared to control SM levels (not shown).

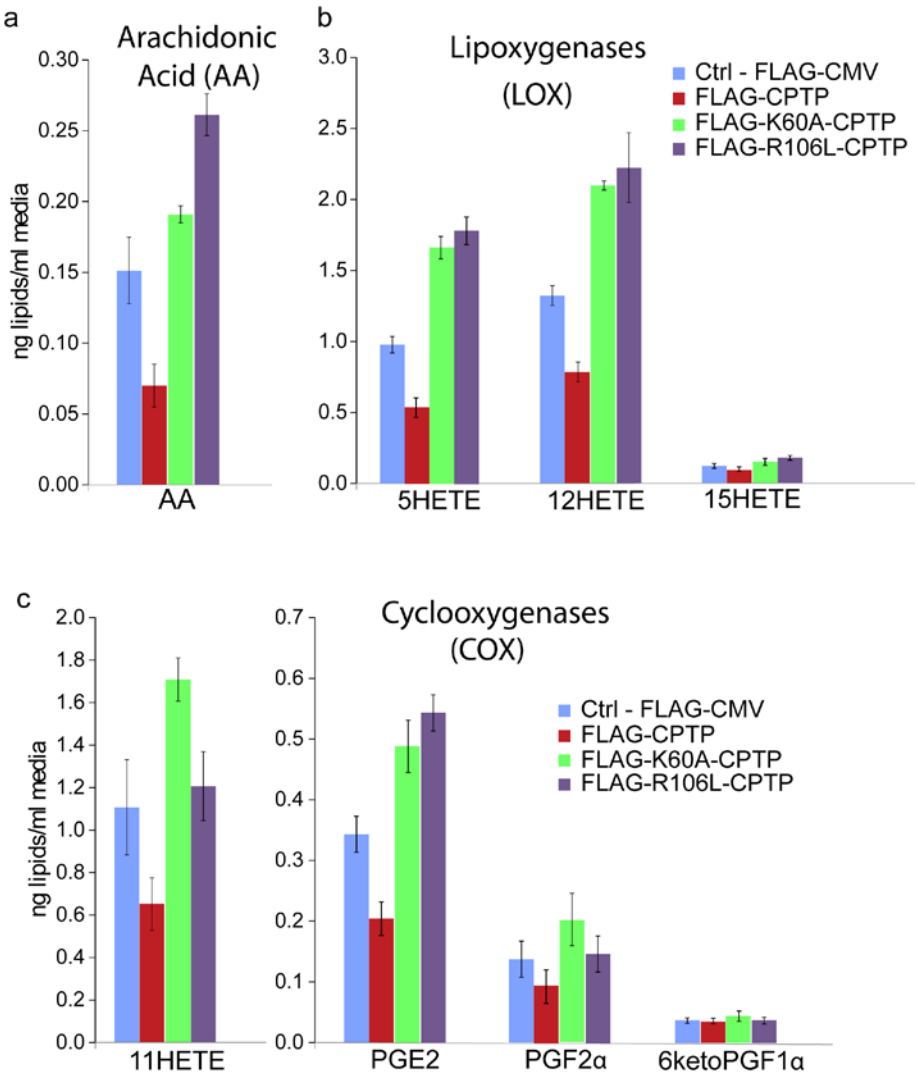

Figure S14. Effect of CPTP and mutant CPTP ectopic expression on arachidonic acid and eicosanoid levels. Secreted lipid levels are expressed in units of nanograms per ml of media by one million cells. **a, b, c,** arachidonic acid (AA) and eicosanoids (LOX and COX pathways). 6keto-PGF1α, the primary prostacyclin metabolite, is nearly unaffected by CPTP overexpression suggesting existence of an arachidonic acid pool derived independently of C1P-activated cPLA$_2$α. Data represent the mean ± s.d. of three independent experiments.